PEGylated Hierarchically Porous Metal−Organic Framework Nanoparticles as Hemoglobin Carriers: Enhancing Colloidal Stability, Biocompatibility and Circulation Time

Weiguang Jin[a], Gizem Bor[a], Mehrdad Asgari[b], Katrine Qvortrup[c], David Fairen-Jimenez[b], Leticia Hosta-Rigau[a,*]

AUTHOR ADDRESS

[a]Department of Health Technology, Technical University of Denmark, 2800 Kongens Lyngby, Denmark

[b]The Adsorption & Advanced Materials Laboratory (A^2ML), Department of Chemical Engineering & Biotechnology, University of Cambridge, Cambridge CB3 0AS, United Kingdom

[c]Department of Chemistry, Technical University of Denmark, 2800 Kongens Lyngby, Denmark

KEYWORDS

Blood Substitutes, Hemoglobin-based Oxygen Carriers, Hierarchical Porous Nanoparticles, Metal-Organic Frameworks

ABSTRACT

Timely blood transfusion is critical for preventing hypoxia and organ failure in cases of acute severe blood loss, yet the current blood supply system faces limitations in availability, storage, and compatibility. To address these challenges, synthetic hemoglobin (Hb)-based oxygen carriers (HBOCs) have emerged as promising substitutes for donor red blood cells (RBCs). However, effective encapsulation strategies that maintain Hb stability, oxygen-binding capacity, and circulation longevity remain a significant hurdle. In this study, we present a novel approach utilizing hierarchically porous UiO-66 metal-organic framework nanoparticles (HP-UiO-66 NPs) to encapsulate Hb, achieving physiologically stable, biocompatible, and functionally efficient synthetic HBOCs. By introducing mesopores within UiO-66 NPs, we enable efficient Hb loading while maintaining micropores for oxygen diffusion. To enhance physiological stability, we employ a catalyst-free click-chemistry surface modification with polyethylene glycol (PEG). The resulting Hb-loaded and PEGylated HP-UiO-66 NPs demonstrate preserved oxygen-binding functionality, excellent colloidal stability in physiological media, and promising biocompatibility in vitro and in vivo. Pharmacokinetic and biodistribution studies confirm prolonged circulation and favorable organ accumulation. These findings establish HP-UiO-66 NPs as a versatile platform for RBC substitutes, advancing the potential biomedical application of metal-organic frameworks for oxygen delivery in critical care settings.

1. INTRODUCTION

Timely transfusion of whole blood or red blood cells (RBCs) is essential for preventing hypoxia and subsequent organ failure in patients suffering from acute severe blood loss. However, the current blood supply system is fraught with challenges—time-consuming matching processes, strict storage requirements, and limited availability—that hinder its effective use in critical scenarios.[1,2] In response to these barriers, researchers have devoted significant efforts to developing synthetic oxygen (O_2) carriers as promising substitutes for RBCs. Among these,

incorporating hemoglobin (Hb), the primary O_2-carrying protein in blood, within delivery vehicles has emerged as a potential solution.[3,4] These so-called Hb-based O_2 carriers (HBOCs) are designed to leverage the O_2-transporting power of Hb while overcoming the toxicity of free Hb, ultimately mimicking the O_2-carrying function of RBCs.[5]

To this end, various strategies have been developed to encapsulate Hb within different carriers such as liposomes,[6] polymersomes,[7] and polymer particles.[8–11] These approaches aim to prevent the dissociation of the Hb tetramer while providing a suitable environment to maintain Hb's functionality. However, despite significant advancements, challenges remain in encapsulating Hb within well-defined structures that preserve its secondary structure and allow for the free diffusion of small molecules, such as O_2 and reducing agents, in and out of the system. Additionally, difficulties in extending the circulation time of these Hb-encapsulating platforms in the bloodstream continue to hinder their clinical translation.[12]

Amidst these challenges, metal-organic frameworks (MOFs), which consist of metal ions connected by organic linkers, have emerged as a promising class of self-assembled materials with remarkable potential for drug delivery and personalized medicine.[13] Thus, MOF nanoparticles (MOF NPs) which feature well-defined, crystalline pore structures with large surface areas have been employed to encapsulate a wide range of therapeutic compounds.[14] However, the vast majority of the approximately 99.000 MOFs discovered to date, feature small micropores (<2 nm), which impede the post-encapsulation of biomacromolecules such as enzymes,[15,16] nucleic acids[17,18] and also Hb.[19,20] While, theoretically, enlarging MOFs pore cages could be achieved by selecting and designing large metal clusters and/or long ligands, the extremely complicated organic synthesis and the lack of structural stability of the resulting MOF NPs restrict their practical utility.[21] Another strategy to bypass MOFs small pore size is by an in situ encapsulation approach in which the biomolecules to be encapsulated act as heterogeneous nucleation seeds and trigger MOF formation.[22] Although the pore size

becomes irrelevant with this method, such strategy is only applicable to the very limited number of MOFs that can be fabricated in biofriendly conditions which mainly include the zeolitic imidazolate framework (ZIF) series, such as ZIF-8 and ZIF-90.[23–29] However, this MOFs subclass is prone to decomposition in physiological conditions leading to the premature rapid release of the encapsulated cargo.

Recently, a defect formation strategy to create MOF NPs with larger pores has been reported.[30] The method involves using UiO-66, a MOF constituted by Zr^{4+} and 1,4-benzene-dicarboxylate (BDC) as the organic ligand, that exhibits a crystalline structure with microporous cages.[31] The fabrication of UiO-66 containing not only micropores but also mesopores (2-50 nm in size), involves the self-assembly of Zr^{4+} and insufficient amounts of the BDC ligand using an alkyl monocarboxylic acid as modulator.[30] The resulting hierarchically porous (HP) UiO-66 NPs (HP-UiO-66 NPs) are obtained following removal of the modulator by acidic treatment, which results in additional pore space. Importantly, the diameter of these new mesopores can be systematically adjusted by varying the length and concentration of the modulator. However, an important limitation of the reported HP-UiO-66 NPs is their inherent instability in physiologically relevant buffers, probably due to the undesired coordination of the phosphates (present in phosphate buffer saline (PBS), cell media or blood) with Zr nodes.

In this work, we present, for the first time, a HP MOF NP based on UiO-66 that is stable in physiological media and thus is well suited for biomedical applications (**Schematic 1a**). The potential of this platform is thoroughly evaluated in vitro and in vivo as a substitute for RBCs. Such an ambitious goal is achieved by encapsulating Hb withing azide-functional HP-UiO-66 NPs followed by surface-modification with polyethylene glycol (PEG) to enhance stability and biocompatibility (Schematic 1b). To prevent the loss of pre-encapsulated Hb during modification, we employ a catalyst-free click-chemistry reaction — strain-promoted alkyne

azido cycloaddition (SPAAC) — which enables highly-specific conjugation between dibenzylcycloocyne (DBCO) and the azide groups in a very mild synthesis process (Schematic 1c).[32]

The development of physiologically stable HP MOF NPs represents a significant step forward in the design of synthetic RBC substitutes. By overcoming critical barriers related to stability and encapsulation, this work provides a versatile platform for O_2 delivery and opens new avenues for the biomedical application of MOFs.

2. MATERIALS AND METHODS

2.1. Materials

All purchased chemical reagents and solvents were used without further purification. Zirconium chloride ($ZrCl_4$), 2-amino-1,4-benzenedicarboxylate (DBC-NH_2), dodecanoic acid (DA), *N,N′*-dimethylformamide (DMF), hydrochloric acid (HCl), ethanol (EtOH), potassium hexacyanoferrate ($K_3[Fe(CN)_6]$), *tert*-butyl nitrite (*t*BuONO), azidotrimethylsilane ($TMSN_3$), tetrahydrofuran (THF), acetone, phosphate buffer saline, 4-(2-hydroxyethyl) piperazine-1-ethane-sulfonic acid (HEPES), sodium dithionite (SDT), sodium lauryl sulphate (SLS), sodium chloride (NaCl), potassium hydroxide (KOH), potassium chloride (KCl), deuterium oxide (D_2O), toluene, Dulbecco's modified eagle's medium-high glucose (DMEM), bicinchoninic acid (BCA) assay, fetal bovine serum (FBS) and penicillin/streptomycin were purchased from Merck Life Science A/S (Søborg, DK). CellTiter-Glo has been purchased from Promega Biotech AB (Stockholm, SE). Dibenzocyclooctyne-polyethylene glycol with Mw 2000 (DBCO-PEG) and Cyanine 7 (Cy7) monosuccinimidyl ester (Cy7-monoNHS ester) were brought from BroadPharm (San Diego, US). Mouse serum from CD-1 mice was obtained from Innovative Research (Novi, MI, US). Activated partial thromboplastin time (aPTT) reagent STA®-PTT automate 5 and prothrombin time (PT) reagent STA®-NeoPTimal with an international sensitivity index value of 1.0 were both purchased from Diagnostica Stago

(Asnières, FR). Human complement component C5a DuoSet ELISA was brought from R&D Systems (Minneapolis, US). The RAW 264.7 cell line was obtained from the European Collection of Authenticated Culture Collections (ECACC, Wiltshire, UK).

Hb was extracted from bovine blood bought from SSI Diagnostica A/S (Hillerød, DK). Human blood was withdrawn from healthy donors at DTU-Health Technology at the Technical University of Denmark (Lyngby, DK) and the withdrawal procedure was performed following approval and in accordance with the guidelines from the Regional Research Ethics Committees of Denmark. Human blood plasma was collected from the supernatant of donor blood.

PBS buffer (pH 7.4) consisted of 10 mM phosphate buffer, 140 mM NaCl and 3 mM KCl dissolved in ultrapure Mili-Q water (MQ); HEPES buffer (pH 7.4) is composed of 20 mM HEPES in MQ; saline is made of a 0.9% NaCl aqueous solution.

2.2. Hb Extraction

The extraction of Hb was conducted following our previously reported protocol.[4] Briefly, the bovine blood was mixed gently with an equivalent volume of saline and centrifuged (1500*g*, 20 min). The supernatant was discarded and the pellet containing the RBCs was thoroughly washed by repeating this procedure two times. The pellet was then suspended in toluene and MQ at volume ratio of 1:0.4:1 and placed into a tapping separatory funnel overnight at 4 °C to allow for the separation of the two phases. The bottom phase containing a clear stroma-free Hb was collected and spun down (8000*g*, 20 min) and the resulting supernatant containing Hb was filtered with disposable polyethylene frits and a diatomaceous earth filter funnel (Chemglass Life Sciences, US) with a vacuum pump. The Hb-containing filtrate was stored in the freezer at −80 °C for further use. The Hb concentration was quantified by a BCA assay.

2.3. Fabrication of UiO-66-based NPs

2.3.1. Synthesis of amino-modified UiO-66 NPs (UiO-66-NH_2 NPs). UiO-66-NH_2 NPs were fabricated following a previous report with minor modifications.[30] Typically, $ZrCl_4$ (160 mg, 0.678 mmol) and BDC-NH_2 (124 mg, 0.686 mmol) were ultrasonically dissolved in DMF (30 mL) using a Pyrex tube. The resulting yellow mixture was then heated in an oven at 120 °C. After 24 h of reaction, the UiO-66-NH_2 NPs were harvested by centrifugation (11 000*g*, 10 min) and successively washed with DMF, acetone and EtOH (3×, 11 000*g*, 10 min) followed by vacuum drying. This procedure typically yielded ~275 mg UiO-66-NH_2 NPs. The successful synthesis was confirmed by the crystal pattern aligning with the simulated one of UiO-66 (**Figure S1**, Supporting Information).

2.3.2. Synthesis of hierarchically porous UiO-66-NH_2 NPs (HP-UiO-66-NH_2 NPs). HP-UiO-66-NH_2 NPs were prepared following a previous report with some modifications.[33] Specifically, a mixture of $ZrCl_4$ (400 mg, 1.715 mmol) and excess DA (12 g, 60 mmol) was ultrasonically dissolved in DMF (100 mL) for 30 min followed by the addition of DBC-NH_2 (150 mg, 0.8574 mmol). The mixture was further sonicated for 30 min to form a yellow uniform solution, which was heated in an oven at 120 °C for 24 h. Next, the pellet was collected by centrifugation and washed with DMF (3×, 11 000*g*, 5 min). DA was removed by immersing the obtained yellow pellet in DMF (100 mL) containing HCl (0.5 mL, 37%) at 90 °C for 12 h. Next, the pellet was spun down (11 000*g*, 5 min), the supernatant was discarded and the HCl treatment was repeated. The product was collected by centrifugation (11 000*g*, 5 min) and washed sequentially with DMF, acetone and EtOH (3×, 11 000*g*, 5 min). After overnight vacuum drying, ~428 mg of yellow powder of HP-UiO-66-NH_2 NPs was obtained.

2.3.3. Synthesis of azido-modified HP-UiO-66 NPs (HP-UiO-66-N_3 NPs). HP-UiO-66-NH_2 NPs (50 mg) were placed in a 25 mL round-bottom flask and ultrasonically dispersed in THF (10 mL). Next, a mixture of *t*BuONO (0.4 mL) and $TMSN_3$ (0.35 mL) was added dropwise

within 5 min. The flask was then placed in an ice bath for overnight stirring with a speed of 400 rpm. After centrifugation, the obtained solid was subsequently washed with THF (10 mL, 3×, 11 000*g*, 5 min) and acetone (10 mL, 3×, 11 000*g*, 5 min). After overnight vacuum drying, ~45 mg of HP-UiO-66-N_3 NPs were obtained.

2.3.4. Pore activation of UiO-66-based NPs. To exchange the residual solvent in the pores of the as-prepared UiO-66-based NPs (i.e., UiO-66-NH_2, HP-UiO-66-NH_2 and HP-UiO-66-N_3 NPs), ~150 mg was soaked sequentially in EtOH (100 mL) and acetone (100 mL) at 50 °C for 48 h each. Next, the NPs were spun down (11 000*g*, 5 min) and placed in uncovered glass vials after discarding the supernatants. The NPs were heated overnight at 140 °C in an oven under vacuum, the glass vials were then tightly closed and cooled down at ambient conditions.

2.3.5. Hb loading and quantification. Activated HP-UiO-66-NH_2 or HP-UiO-66-N_3 NPs (5 mg) were incubated with Hb solutions (0.5 mL, 1, 2, 4, 6, 8, 10, 14 and 20 mg mL^{-1} in HEPES buffer) under continuous shaking at 1000 rpm for 2 h. Next, the NPs were collected by spinning down and washed in MQ (13 500*g*, 5 min). The resulting Hb-loaded HP-UiO-66-NH_2 NPs (Hb@HP-UiO-66-NH_2 NPs) or HP-UiO-66-N_3 NPs (Hb@HP-UiO-66-N_3 NPs) were dispersed in MQ for further studies. The amount of non-entrapped Hb was assessed using a previously reported SLS-Hb assay.[34] In brief, the supernatants (10 µL) after the first spinning cycle were mixed with SLS (100 µL, 0.6 mg mL^{-1} in MQ) in a 96-well plate (NunclonTM Delta Surface). In parallel, different dilutions of the Hb stock obtained from bovine blood were prepared in HEPES to serve as standards. The plate was covered with aluminum foil and incubated on a plate shaker for 5 min and the absorbance (Abs) at 412 nm was recorded using a Nanodrop 2000c spectrophotometer (Thermo Fisher Scientific, Waltham, MA, US). The Abs readings were conducted in triplicate. The standard curve was created by plotting the average reading of each Hb standard versus the concentration in mg mL^{-1}.

The concentration of Hb present in the supernatants (unentrapped Hb) was determined by interpolation into the standard curve. The amount of encapsulated Hb was quantified by subtracting the amount of non-entrapped Hb from the known initial amount. The Hb entrapment efficiency (EE) and loading content (LC) were calculated using the following formulas:

EE = (encapsulated Hb amount/initial amount of Hb) × 100

LC = (encapsulated Hb amount/total amount of final sample) × 100

2.3.6. Synthesis of PEGylated Hb@UiO-66-N_3 NPs (Hb@HP-UiO-66-PEG NPs). DBCO-PEG (20 mg in 0.5 mL MQ) was added to Hb@HP-UiO-66-N_3 NPs (10 mg in 0.5 mL MQ) placed in a 2 mL Eppendorf tube and the resulting mixture was incubated in a thermoshaker at room temperature (1000 rpm, 1 h) and kept in a refrigerator for overnight. The suspension was spun down (12 000*g*, 5 min) and washed with MQ (2 mL, 3×, 12 000*g*, 5 min). The resulting Hb@HP-UiO-66-PEG NPs were dispersed in MQ for further studies.

2.4. Physiochemical Characterization

2.4.1. NMR. ^{1}H-NMR spectra were recorded on a Bruker Avance spectrometer (Bruker, Billerica, US) with a prodigy cryoprobe operating at 400 MHz. The NPs were placed in 2 mL glass vials and dried in a vacuum oven at 50 °C overnight. The resulting powder (~10 mg) was dissolved in KOH (2 M in 0.5 mL D_2O) and heated at 80 °C for 1-2 h to digest the NPs. Afterwards, the suspensions were spun down (12 000*g*, 10 min) and the supernatants containing the organic components of the NPs were transferred to an NMR tube for NMR monitoring.

2.4.2. Powder X-ray diffraction (PXRD). The PXRD spectra were collected using a benchtop diffractometer (Malvern Panalytical Ltd., Malvern, UK) with a 2θ range from 4 to 50° at 298 K using Cu radiation. The simulated PXRD pattern of UiO-66 was generated with the Mercury program based on the reported crystal information.[35]

2.4.3. Fourier transform infrared (FTIR) spectroscopy. FTIR spectroscopy analysis was performed using an ALPHA-P spectrometer (Bruker, Billerica, US) with a spectral resolution of 2 cm^{-1}. Prior to the measurement, the NPs were dried at 50 °C in a vacuum oven and gently pressed into fine powder using a sample spoon. The powdered NPs were then placed at the center of an FTIR sample stage to cover the crystal detector and the measurement was performed at ambient conditions. Background calibration was conducted for each analysis.

2.4.4. Scanning electron microscopy (SEM). SEM micrographs were obtained using a Quanta 200 field emission gun scanning electron microscopy (FEI Company, Hillsboro, US). The droplet containing the NPs suspension was mounted onto the conductive silicon wafer on the top of sample holder for ambient drying. The SEM micrographs were taken under vacuum using an accelerated electron beam with a voltage of 10-20 kV. The images were further analyzed using the ImageJ software.

2.4.5. Gas uptake. Nitrogen (N_2) sorption isotherm and pore size distribution measurements were performed on a Micromeritics Tristar Surface Area and Pore Size Analyzer at 77 K. Prior to measurements, NPs (~100 mg) were soaked in EtOH and acetone for 48 h each followed by overnight drying using a vacuum over. Then the dried NPs powders were thoroughly activated to remove residual solvents using a Micromeritics Smart VacPrep system at 140 °C under vacuum for 24 hours (or overnight) while purging with ultra-high-purity N_2. Once activated, the sample was immediately transferred to the analysis system to prevent exposure to atmospheric contaminants. The adsorption isotherms were collected within a relative pressure range (P/P_0) of up to 1 bar, gradually introducing in controlled increments while allowing equilibrium to be reached at each step. The calculation of pore size distribution uses the nonlocal density functional theory (NLDFT) implemented in the Micromeritics software. The Brunauer–Emmett–Teller (BET) areas were calculated using BETSI based on the extended Rouquerol criteria.[36]

2.4.6. Zeta (ζ)-potential, hydrodynamic size and polydispersity index (PDI). The ζ-potentials, hydrodynamic size and PDI of free Hb and the different UiO-66-based NPs were obtained using a Zetasizer nano ZS instrument (Malvern Instruments Ltd., Malvern, UK) under ambient conditions. Free Hb and the different NPs were adequately dispersed with a 100× dilution in MQ for size and PDI analysis and in HEPES buffer for ζ-potential measurement. Each measurement was conducted in triplicate and the results are expressed as mean ± SD.

2.4.7. Transmission electronic microscope (TEM). TEM imaging was conducted using a Tecnai T20 G2 (FEI Company, Hillsboro, US) equipped with a high-tension voltage of 200 keV under vacuum. A droplet containing the NPs suspension was applied onto the glow discharged lacey carbon film Cu TEM grid (300 Mesh) and dried at ambient conditions. The grid was then loaded on the single Tilt holder to collect the TEM images in bright field. The images were further analyzed using the ImageJ software.

2.5. O_2-Transporting Properties

2.5.1. Reversible O_2-binding and release. The ability of free Hb and NPs to reversibly bind and release O_2 was evaluated by UV-vis spectroscopy. For that, free Hb and the NPs (i.e., Hb@HP-UiO-66-NH_2 NPs) were suspended in MQ and the UV-vis spectra in the wavelength range of 350−600 nm was recorded using a UV-2600 UV−vis spectrophotometer (Shimadzu, Kyoto, JP). To obtain deoxygenated Hb (deoxy-Hb), a pinch of the O_2 scavenger SDT was added, and the suspensions were purged with N_2 for 10 min followed by recording the UV-vis spectra. Next, the suspensions were purged with an air flow for 10 min to obtain oxygenated Hb (oxy-Hb) and the corresponding UV-vis spectra was recorded.

2.5.2. Quantification of released O_2. The amount of O_2 released by the different NPs was evaluated using a needle-type O_2 meter (PreSens, Regensburg, DE). For that, free Hb (1 mg in 600 μL MQ) and the different NPs (i.e., Hb@HP-UiO-66-NH_2, Hb@HP-UiO-66-N_3 and Hb@HP-UiO-66-PEG NPs) (their tested amounts were adjusted relative to 1 mg of Hb, 600

μL MQ) were placed into a glass vial tightly sealed with a rubber cap. The needle probe was inserted into the rubber cap and the release of O_2 from oxy-Hb was forced by the addition of a solution of $K_3[Fe(CN)_6]$ (100 μL, 10 wt%). The amount of released O_2 was determined by subtracting the maximum value observed after the addition of $K_3[Fe(CN)_6]$ from the value measured before the $K_3[Fe(CN)_6]$ solution was added. The data was then normalized to the O_2 released from the same amount of free Hb.

2.6. Assessment of NPs Stability

The NPs (i.e., Hb@HP-UiO-66-NH_2 and Hb@HP-UiO-66-PEG NPs) (~5 mg) were incubated in different biologically relevant fluids (2 mL of saline, HEPES, mouse serum, human blood plasma, DMEM and PBS) at 1000 rpm and 37 °C using a thermoshaker. NPs in MQ incubated without shaking at room temperature was used as the negative control. At predefined time intervals, the NPs suspension was diluted 20× with the corresponding buffer for hydrodynamic size measurement and with MQ for SEM analysis. Diluting the NPs suspension in MQ is crucial for SEM analysis because it can alleviate the background interference caused by buffer components and facilitate the NPs imaging. For PXRD analysis, the NPs were spun down (12 000*g*, 10 min), washed with MQ (1×, 2 mL, 12 000*g*, 10 min) and freeze-dried.

2.7. Biocompatibility

2.7.1. Cell Culture. RAW 264.7 cells were cultured in DMEM supplemented with 10% (v/v) FBS and 1% penicillin/streptomycin mixture at 37 °C with 5% CO_2. The cells were harvested prior to reaching 80–90% confluence.

2.7.2. Cell Viability (CV). CV was assessed using the CellTiter-Glo assay after 24 h of treatment with Hb@HP-UiO-66-PEG NPs. Briefly, RAW 264.7 cells were seeded in a 96-well plate at a density of 3×10^4 cells per well and incubated for 24 h at 37 °C with 5% CO_2 in a humidified atmosphere. The cells were then washed with PBS (1×) and exposed to Hb@HP-UiO-66-PEG NPs at concentrations ranging from 0.01 to 1 mg mL^{-1}. After 24 h of treatment,

the cell media was replaced with 100 µL of a mixture of fresh cell media and CellTiter-Glo reagent at 1:1 volume ratio. The well plate was then covered with aluminum foil, shaken for 5 min, and incubated at room temperature for 10 min. After incubation, 95 µL from each well was transferred to a white 96-well plate (Nunclon™ Delta Surface Flat White) and the luminescence was measured using a Tecan Spark microplate reader (Tecan Group Ltd, Männedorf, CH) with and integration time of 0.25–1 sec per well. Untreated cells and cell media only served as positive and negative controls, respectively. The results are expressed as normalized CV (nCV), representing the relative percentage of viable cells compared to untreated controls. The calculation using the following formulas:

nCV (%) = (Abs experimental value – Abs negative control)/(Abs positive control – Abs negative control) × 100

2.7.3. Hemolysis rate. Human whole blood, which was collected in heparin-coated tubes, was centrifuged to precipitate the RBCs and washed with pre-cold PBS (3×, 1000*g*, 15 min, 4 °C). Next, the resulting pellets containing the RBCs (1 mL) were diluted with PBS (49 mL) in a 50 mL falcon tube. The diluted RBCs suspension (200 µL) was incubated with the different NPs (0.001, 0.01, 0.05, 0.1, 0.25, 0.5, 1 mg mL^{-1} in 300 µL PBS) using a Thermoshaker (1000 rpm, 3 h, 37 °C). The diluted RBC suspension incubated with PBS (300 µL) and MQ (300 µL) only were used as positive and negative controls, respectively. After incubation, the NPs were removed by spinning down (1000*g*, 10 min) and the RBCs-containing supernatants were collected and spun down again at a higher speed (12 000*g*, 10 min). These new supernatants containing any potential released Hb were transferred to a 96-well plate and the Abs signal at 540 nm was recorded using a multimode plate reader (Tecan Spark, Tecan Group Ltd, Männedorf, CH). The hemolysis rate was calculated with the following equation:

Hemolysis rate (%) = (Abs of samples – Abs negative control)/(Abs positive control – Abs negative control) × 100.

Meanwhile, the RBCs-containing pellet after the first centrifugate cycle was resuspended in PBS and the RBCs morphology was assessed using an Axiovert 25 inverted microscope (Carl Zeiss A/S, Birkerød, DK) with a 32× magnification.

2.7.4. Plasma Coagulation. The effect of Hb@HP-UiO-66-PEG NPs on the extrinsic and intrinsic blood coagulation pathways was estimated by PT and aPTT assay, respectively.[37] Human whole blood was spun down (1500*g*, 15 min) and the supernatant was collected to afford platelet-poor plasma (PPP). Then the NPs were mixed with the obtained PPP at volume ratio of 1:9, resulting in the final concentrations ranging between 0.04 and 1 mg mL^{-1}, and incubated at 37 °C for 30 min. The PPP incubated with PBS (pH 7.4) only was employed as negative control. Subsequently, Merlin MC1 coagulometer (Merlin Medical, ABW Medizin und Technik, Lemgo, DE) was used to assess the PT and aPTT and the reagents from supplier (Diagnostica Stago, Asnières, FR) to induce the extrinsic and intrinsic coagulation cascades were used for PT and aPTT, respectively.

2.7.5. Complement Activation. Complement activation was evaluated following a reported protocol.[38] Complement protein C5a level was assessed employing the human complement component C5a DuoSet ELISA assay. In brief, Hb@HP-UiO-66-PEG NPs (6 mg mL^{-1} in 50 µL PBS) were gently mixed with human blood plasma (250 µL) and incubated using a thermoshaker (37 °C, 30 min). After spinning down the NPs (4000*g*, 5 min, 4 °C), the Abs at 450 nm of the collected supernatants were recorded using the plate reader (Tecan Spark, Tecan Group Ltd, Männedorf, CH). The standards from the suppliers were used to create a standard curve. In addition, plasma with PBS only (pH 7.4) and complement activator zymosan (0.2 mg mL^{-1} in blood plasma) served as background and positive control, respectively.

2.8. In Vivo Studies

2.8.1. Hb labelling with Cy7. Hb (50 mg) was dissolved in $NaHCO_3$ (0.1 M in 10 mL MQ, pH 9) followed by the dropwise addition of Cy7 (5 mg dissolved in 500 µL DMSO). The

mixture was gently stirred using a magnetic stirrer (300 rpm, 4 h) in the dark. Next, unreacted Cy7 was eliminated by filtering the solution with a 30 kDa Amicon Ultra filter. The green pellet containing Cy7-labelled Hb (Hb^{Cy7}) was harvested by washing with MQ (3×, 5000*g*, 5 min) and the concentration was quantified by SLS assay as described in section 2.3.5.

2.8.2. Fabrication of Hb^{Cy7}-loaded HP-UiO-66-PEG NPs (Hb^{Cy7}@HP-UiO-66-PEG NPs). 10 mg of activated HP-UiO-66-N_3 NPs were immersed in a Hb^{Cy7} solution (10 mg mL^{-1} in 1 mL MQ) and incubated using a thermoshaker (1000 rpm, 2 h). The resulting green pellet containing Hb^{Cy7}-loaded HP-UiO-66-N_3 NPs (Hb^{Cy7}@HP-UiO-66-N_3 NPs) was collected by spinning down and washed in MQ (3×, 12 000*g*, 5 min). Next, the pellet was suspended in MQ (0.5 mL) and PEGylation was conducted by adding DBCO-PEG (20 mg in 0.5 mL MQ) followed by continuous shaking using the thermoshaker (1000 rpm, 1 h). The resulting Hb^{Cy7}@HP-UiO-66-PEG NPs were harvested by spinning down and washed with MQ (2 mL, 3×, 12 000*g*, 5 min).

2.8.3. Animal Model. Healthy male CD-1 mice (6-8 weeks old, body weight 35-40 g) purchased from Charles River Laboratory (Sulzfeld, DE) were used for animal studies. The mice were housed in polypropylene cages within an air-conditioned animal facility, where the temperature was set at 23 ± 3 °C, the relative humidity to 40-70% and 12 h light/dark cycle with ad libitum access for feed. All animal experimental procedures were approved by the Danish National Animal Experiment Inspectorate.

2.8.4. Pharmacokinetics. To assess the blood clearance profile, the pharmacokinetic (PK) parameters of Hb^{Cy7}@HP-UiO-66-PEG NPs after animal injection were evaluated. For that, the NPs (100 µL) were intravenously injected into the lateral tail vein of mice at a single dose of 10 mg kg^{-1} and sterile PBS (100 µL, pH 7.4) was used as a control (n = 3 per group, per time point). Next, blood samples were collected from the opposite lateral tail vein at different time intervals (0.5, 1, 4, 6, 8, 10, 12, and 24 h) and centrifuged (2000*g*, 10 min, 4 °C) to collect the

supernatant-containing plasma. The fluorescence intensity (FI) of the supernatant was assessed ($\lambda_{ex}/\lambda_{em}$ = 750/790 nm) using the plate reader and correlated to the NPs standard curve. The theoretical administered concentration was estimated using the total blood volume per mouse which was estimated to be 7.5% of body weight. The PK parameters were estimated by noncompartmental analysis using MATLAB Simbiology version 6.4.1.

2.8.5. Biodistribution studies. Fluorescently labeled Hb^{Cy7}@HP-UiO-66-PEG NPs were intravenously injected into the lateral tail vein of CD-1 mice (n = 3 per group, per time point) at a single dose of 10 mg kg^{-1} in a total volume of 100 µL. Control mice (n = 3) received the same volume of sterile PBS (pH 7.4). At designated time points (0.5, 1, 4, 8, and 24 h), mice were anesthetized with intraperitoneal injections of Midazolam (50 mg kg^{-1}; Hameln, Glostrup, DK). The liver, brain, intestines, spleen, heart, lungs, and kidneys were then collected and imaged using a fluorescence molecular tomography device (U-CT OI, MILabs B.V., Utrecht, NL) in 2D reflectance imaging mode ($\lambda_{ex}/\lambda_{em}$ = 710/785 nm). The fluorescence signal from manually defined regions of interest was quantified using MILabs OI Post Processing v2.4.1 software (MILabs B.V., Utrecht, NL). The data was reported as mean ± SD, with all organs imaged under consistent instrument settings.

2.9. Statistics

Statistical analyses were performed using one-way ANOVA (95% confidence level, α =0.05) in GraphPad Prism (10.0.2) followed by the Kruskal-Wallis multiple comparison test (*p<0.05, **p<0.005, ***p<0.001, ****p<0.0001).

3. RESULTS AND DISCUSSION

3.1. Fabrication of HP-UiO-66-NH_2 NPs

MOF NPs hold great promise to serve as delivery vehicles for small molecule drugs thanks to their tunable chemical properties and intrinsic porosity.[39,40] However, the vast majority of

MOFs display cages within the microporous regime which significantly limits their ability to load large biomolecules.[41] Consequently, despite their potential, only a solitary example of Hb encapsulation within pre-synthesized MOF NPs has been reported.[42] In particular, our group pioneered the use of the so-called porous coordination network (PCN)-333(Al), which is based on trivalent aluminum ions. PCN-333(Al) exhibits one of the highest void volumes and largest cages among MOFs, enabling Hb encapsulation.[12,42,43] However, a notable limitation of PCN-333(Al) is the limited stability in aqueous solvents and the potential toxicity of the aluminum component, posing challenges for its clinical translation.[44,45]

MOF structural defect engineering is an emerging promising strategy to overcome these limitations by creating hierarchically porous structures. These structures facilitate the encapsulation of macromolecular compounds, such as Hb, within newly formed mesopores while preserving the inherent micropores for O_2 diffusion in and out of the system. **Schematic 1a** depicts the synthesis of amino-modified HP-UiO-66-NH_2 NPs. To generate mesopores, DA was introduced as a competitive ligand for the partial coordination of Zr^{4+} prior to the solvothermal synthesis of UiO-66-NH_2 NPs with DBC-NH_2.[2] The resulting DA-containing UiO-66-NH_2 NPs (DA-UiO-66-NH_2 NPs) were treated with HCl to remove the modulator, yielding HP-UiO-66-NH_2 NPs displaying both meso- and micropores. ^{1}H-NMR spectroscopy was employed to monitor the synthesis process (**Figure 1a**). DA-UiO-66-NH_2 NPs exhibited characteristic ^{1}H-NMR peaks of DA (2.1, 1.4, 1.2 and 0.75 ppm, **Figure S2**, Supporting Information) and DBC-NH_2 (in the range of 6-8 ppm, **Figures S3-S5**, Supporting Information). Following HCl treatment, the disappearance of DA's characteristic peaks confirmed its successful removal. PXRD patterns for both DA-UiO-66-NH_2 and HP-UiO-66-NH_2 NPs exhibited peaks at 2θ = 7.3, 8.4 and 25.7°, corresponding to the (111), (222) and (600) crystal planes, respectively (Figure 1b). These patterns aligned perfectly with the simulated UiO-66 structure, confirming that the crystal phase purity and topological structure remained intact

despite the incorporation and removal of DA. SEM micrographs revealed that both DA-UiO-66-NH_2 and HP-UiO-66-NH_2 NPs displayed spherical morphologies with a uniform size distribution of ~100 nm, making them well-suited for intravenous applications (Figure 1c, **S6** and **S7**, Supporting Information).[46,47] TEM analysis showed bright, spot-like pores distributed throughout both types of NPs, which is consistent with their porous structures (Figure 1d). Interestingly, TEM imaging also revealed rougher edges on HP-UiO-66-NH_2 NPs compared to the smooth edges of DA-UiO-66-NH_2 NPs. We attribute this roughness to structural defects resulting from DA removal.

The formation of mesopores within the as-prepared HP-UiO-66-NH_2 NPs was next verified through N_2 adsorption-desorption isotherms (**Figure 2a**). Pristine UiO-66-NH_2 NPs displayed a typical Type I sorption curve, characterized by high N_2 adsorption near saturation at relatively low pressure, consistent with their predominantly microporous structure. Pore size distribution analysis revealed pore sizes ranging from 0.5 to 1.6 nm, aligning with expectations for microporous UiO-66-NH_2 NPs (Figure 2b). In contrast, HP-UiO-66-NH_2 NPs exhibited a sorption curve that combined Type I and Type IV patterns, along with a significantly higher sorption capacity. The presence of a hysteresis loop in the desorption branch at relative pressures of 0.8–1.0 further confirmed the introduction of mesopores (Figure 2a). Pore size distribution analysis clearly demonstrated the presence of mesopores ranging from 2 to 20 nm, in addition to the inherent micropores (Figure 2b). Furthermore, a slight increase in the BET area was observed when comparing HP-UiO-66-NH_2 NPs (1069 m^2 g^{-1}, Figure **S8** and **S9**, Supporting Information) with UiO-66-NH_2 NPs (964 m^2 g^{-1}, Figure **S10** and **S11**, Supporting Information), aligning with the formation of mesopores. Overall, these results unequivocally validate the successful creation of mesopores within HP-UiO-66-NH_2 NPs, highlighting their potential to overcome pore size limitations and enable the efficient encapsulation of Hb.

3.2. Hb Encapsulation and O_2 Transporting Ability

Next, Hb-loaded NPs, Hb@HP-UiO-66-NH_2 NPs, were fabricated by incubating Hb with HP-UiO-66-NH_2 NPs (**Figure 3a**). The successful encapsulation was visually confirmed by a color change from yellow (for HP-UiO-66-NH_2 NPs) to red, a characteristic hue of Hb. EE and LC evaluation revealing the expected decrease in EE and an increase in LC with higher Hb concentrations, reaching a plateau of ~20% LC at an input Hb concentration of 10 mg mL^{-1} (Figure 3b). Based on these findings, this concentration was chosen for the next experiments. N_2 adsorption-desorption isotherms revealed a significant reduction in N_2 uptake for Hb@HP-UiO-66-NH_2 NPs, while the position of the isothermal knee at relative low pressure remained largely unchanged (Figure 3c). This suggests that, as expected due to its size (~5 nm), Hb primarily fills the mesopores rather than the micropores. Pore size distribution analysis further corroborated this, showing a notable reduction in mesopore volume (Figure **S12**, Supporting Information). While HP-UiO-66-NH_2 NPs displayed a BET area of 1069 m^2 g^{-1} (Figure S8 and S9, Supporting Information), Hb@HP-UiO-66-NH_2 NPs showed a lower BET area of 860 m^2 g^{-1} m (Figure **S13** and **S14**, Supporting Information), also confirming the successful Hb encapsulation. These results validate the creation of mesopores within HP-UiO-66-NH_2 NPs as an effective strategy for Hb entrapment.

The physiochemical properties of Hb@HP-UiO-66-NH_2 NPs were further characterized. ζ-potential measurements demonstrated a shift from +48.7 mV for HP-UiO-66-NH_2 NPs to +35.6 mV for Hb@HP-UiO-66-NH_2 NPs upon encapsulation of negatively charged Hb (-36.7 mV) (Figure 3d), suggesting charge complementarity contributed to loading alongside pore size selection.[48] SEM micrographs confirmed that Hb@HP-UiO-66-NH_2 NPs retained their spherical morphology and uniform size (~100 nm) (Figure 3e and **S15**, Supporting Information), while TEM analysis revealed smoother edges compared to HP-UiO-66-NH_2 NPs, potentially due to mesopore filling (Figure 3f and **S16**, Supporting Information). PXRD

patterns confirmed that the crystal structure remained intact(Figure 3g), demonstrating excellent structural stability throughout the encapsulation process.

Maintaining the O_2-carrying functionality of Hb is essential for designing HBOCs. As illustrated in Figure 3h, free Hb exhibited reversible spectral shifts during O_2 release and binding cycles, as shown by UV-vis spectroscopy. The Soret peak (~412 nm) and Q-band peaks (541 and 577 nm) indicated oxy-Hb, while deoxygenation (with the addition of an O_2 scavenger) shifted the Soret peak to ~430 nm and merged the Q-bands into a single peak at 557 nm, indicating the formation of deoxy-Hb. Next, the UV-vis spectrum returned to its initial oxygenated state after additional air purging. These spectral changes were reversible upon reoxygenation. Similarly, Hb@HP-UiO-66-NH_2 NPs displayed the Soret peak characteristic of oxy-Hb (Figure 3i), with reversible spectral shifts confirming preserved O_2-binding functionality (Figure 3j). Quantification using an O_2 electrode demonstrated an increase of ~15.1 Torr in O_2 levels upon the addition of $K_3[Fe(CN)_6]$, indicating O_2 release from the encapsulated Hb (Figure 3k). This indicates that approximately 55% of the encapsulated Hb remained functional for O_2 binding, compared to free Hb (Figure **S17**, Supporting Information). These findings collectively demonstrate the capability of Hb@HP-UiO-66-NH_2 NPs to serve as effective O_2 carriers.

3.3. Phosphate Ions Destabilize Hb@HP-UiO-66-NH_2 NPs in Physiologically Relevant Media

To evaluate the colloidal stability of Hb@HP-UiO-66-NH_2 NPs, we assessed their structural integrity under physiologically relevant conditions. Stability in such environments is crucial for the effective delivery and therapeutic efficacy of newly developed HBOCs. Thus, as a first step, we screened the effect of different physiologically relevant solutions (i.e., PBS, DMEM, HEPES and saline) on the crystallinity of Hb@HP-UiO-66-NH_2 NPs after incubation for 24 h at 37 °C (**Figure 4a**). When compared to MQ water, which served as a negative control, the

PXRD patterns demonstrated that the crystal structure remained intact in saline and HEPES buffer. However, the results were different for Hb@HP-UiO-66-NH_2 NPs incubated in DMEM and PBS where the diffractograms display broad halos instead of sharp, well-defined peaks, indicating loss of crystallinity and the development of an amorphous phase. We attribute this instability to the presence of phosphate ions in both DMEM and PBS, which likely coordinate the Zr clusters of UiO-66 —a well-documented phenomenon observed in other MOFs[49–51] — leading to Hb@HP-UiO-66-NH_2 NPs decomposition. Next, the impact of the phosphate ions on the colloidal stability and morphology of Hb@HP-UiO-66-NH_2 NPs was evaluated by DLS and SEM, respectively. Time-resolved DLS measurements revealed a rapid increase in NP size after only 5 min of PBS incubation, followed by continued growth over 1 h while, at 12 h of incubation, the size distribution peak becomes significantly broader and multiple peaks emerge indicating NP aggregation or fusion (Figure 4b). SEM imaging further confirmed these observations, showing pronounced morphological changes after 2 h of PBS exposure, including significant edge etching and an overall increase in NP size (Figure 4c) compared to those in MQ (Figure 3e). Collectively, these findings indicate that while Hb@HP-UiO-66-NH_2 NPs exhibit good stability in saline and HEPES, they undergo rapid degradation in DMEM and PBS due to phosphate-induced structural breakdown. This highlights the need for further modifications to enhance their stability in physiologically relevant conditions.

3.4. Surface Functionalization with PEG

The inherent instability of Hb@HP-UiO-66-NH_2 NPs in phosphate-containing media impedes their in vivo applicability. In addition to being colloidally stable, nanoparticulated HBOCs should also display biocompatibility and extended circulation times once administered in the body. Thus, we next decided to surface functionalize Hb@HP-UiO-66-NH_2 NPs with PEG in an attempt to protect them from phosphate degradation but also to minimize the adsorption of plasma proteins (opsonization), which typically mark foreign NPs for immune clearance. The

stealth effect promoted by PEG reduces immune recognition and enhances circulation time without triggering an inflammatory response.[52,53]

To generate PEGylated Hb@HP-UiO-66-NH_2 NPs, a facile click-chemistry reaction was adopted to avoid chemical modification of the encapsulated Hb which will result in compromised functionality (i.e., altered O_2 binding and releasing properties) (**Figure 5a**). Specifically, in the presence of *t*-butyl nitrite and trimethylsilyl azide, the primary amines in HP-UiO-66-NH_2 NPs were converted to azide groups, resulting in HP-UiO-66-N_3 NPs (Schematic 1b). Following loading with Hb to form Hb@HP-UiO-66-N_3 NPs, surface PEGylation was achieved via SPAAC employing DBCO-modified PEG, which is a copper-free process that can be conducted in aqueous solvent and at mild temperature (Schematic 1c). The formation of PEGylated Hb@HP-UiO-66-PEG NPs was verified using FTIR and NMR. The successful conversion of amines to azide groups in HP-UiO-66-N_3 NPs was confirmed by FTIR as shown in Figure 5b by the peak at 2122 cm^{-1} which is characteristic of asymmetric azide stretching and was not present within the precursor HP-UiO-66-NH_2 NPs. Importantly, this azide peak persisted after Hb encapsulation but disappeared post-PEGylation. This result confirms the successful PEGylation via azide−DBCO conjugation. Additionally, the FTIR spectrum of Hb@HP-UiO-66-PEG NPs revealed methylene (-CH_2-) and ether bone (-O-) signals at 2883 and 1097 cm^{-1}, respectively, which can be attributed to DBCO-PEG. Comparative ^1H NMR spectra provided further evidence, with a distinct signal at 3.53 ppm, corresponding to PEG's oxyethylene groups, present only in Hb@HP-UiO-66-PEG NPs (Figure 5c).

Mesopores within HP-UiO-66-N_3 NP_S were confirmed using N_2 adsorption-desorption isotherms and pore size distribution analysis, showing minimal impact from azide modification (Figure **S18** and **S19**, Supporting Information). Similar EE and DL values were obtained when Hb was loaded to create Hb@HP-UiO-66-N_3 NPs as compared to the precursor Hb@HP-UiO

-66-NH_2 NPs, indicating that azide modification did not compromise Hb encapsulation. The Hb loading is also evidenced by the reduction in both N_2 uptake (Figure **S20**, Supporting Information) and BET area (Figure **S21-S24**, Supporting Information) when comparing Hb@HP-UiO-66-N_3 with HP-UiO-66-N_3 NPs. Electrostatic interactions between negatively charged Hb and positively charged Hb@HP-UiO-66-N_3 NPs drove encapsulation, as evidenced by reduction in ζ-potential (Figure 5e). PEGylation caused only a minor ζ-potential shift, reflecting minimal impact on surface charge. Consistent PXRD diffractograms indicated that crystalline was maintained throughout synthesis, demonstrating structural stability (Figure **S25**, Supporting Information). Hydrodynamic size measurements by DLS showed monodisperse distributions, with negligible size changes following Hb encapsulation (i.e., 109.9 ± 5.0 and 114.9 ± 1.8 nm and PDIs of 0.135 and 0.086 for HP-UiO-66-N_3 and Hb@HP-UiO-66-N_3 NPs, respectively). A slight size increase after PEGylation (i.e., 140.8 ± 8.3 nm, PDI of 0.167), indicating successful surface modification (Figure 5f). SEM images confirmed a uniform spherical morphology for Hb@HP-UiO-66-PEG NPs with increased size (Figure 5g, **S26** and **S27**, Supporting Information) while TEM analysis revealed the deposition of a thin layer (up to ~12 nm thick) around the NPs, further confirming successful PEGylation (Figure 5 h).

Importantly, this catalyst-free SPAAC approach avoids harsh conditions and byproducts that could compromise the functionality of pre-encapsulated Hb. Therefore, we assessed the O_2 releasing capacity of Hb@HP-UiO-66-N_3 and Hb@HP-UiO-66-PEG NPs using free Hb as the positive control (Figure 5i). The results demonstrated that approximately 60% of encapsulated Hb remained functional within Hb@HP-UiO-66-N_3 NPs, which is slightly higher than the 55% observed in Hb@HP-UiO-66-NH_2 NPs (Figure S17, Supporting Information). One possible explanation for slight improvement is the weaker electron-donating ability of the azide group within Hb@HP-UiO-66-N_3 NPs compared to the amine group in Hb@HP-UiO-66-NH_2 NPs, leading to reduced interactions with Fe^{2+} in Hb and thereby better preserving its O_2-binding

capacity. Notably, no significant difference was observed between Hb@HP-UiO-66-N_3 and Hb@HP-UiO-66-PEG NPs, indicating that SPAAC-mediated PEGylation efficiently prevents functional loss of Hb during the post-PEGylation of HBOCs. Additionally, the N_2 and BET area decreased after surface PEGylation (Figure S20, **S28** and **S29**, Supporting Information) while the pore size distribution (Figure **S30**, Supporting Information) confirms that Hb@HP-UiO-66-PEG NPs retained their porous nature. This suggests that PEGylation has a minimal impact on the pores, which preserve the pathways for O_2 diffusion. These collectively underscores that mild PEGylation preserves Hb's O_2-binding capacity.

In summary, PEGylation effectively modified the surface properties of the NPs without compromising structural integrity or functionality, supporting its utility in Hb carrier design.

3.5. Enhanced Stability of Hb@HP-UiO-66-PEG NPs in Physiologically Relevant Solvents

To investigate whether surface PEGylation enhances the stability of the as-prepared Hb@HP-UiO-66-PEG NPs, we evaluated the effect of different physiologically relevant solutions (i.e., PBS, DMEM, human plasma, mouse serum, HEPES and saline) on their crystallinity after incubation for 3 and 7 days at 37 °C (**Figure 6a**). Remarkably, when compared to MQ water, which served as a negative control, the PXRD patterns of the Hb@HP-UiO-66-PEG NPs remained intact in all studied solvents after 3 days of exposure (Figure 6ai). Even after 7 days, only very slight amorphousness could be observed for NPs incubated in PBS and DMEM (Figure 6aii). The colloidal stability and morphology of Hb@HP-UiO-66-PEG NPs in phosphate-containing solutions (i.e., PBS and DMEM) was further investigated by DLS and SEM, respectively. Time-resolved DLS analysis confirmed the excellent colloidal stability of Hb@HP-UiO-66-PEG NPs in both buffers (Figure 6b), as their hydrodynamic diameters remained unchanged over the 7-day period (see **Table S1**, Supporting Information for the exact values). Only a slight aggregation (~2.2% proportion) could be detected in PBS. The PDI also

remained remarkably low in both PBS and DMEM, with values below 0.2 after 2 days and around 0.2 after 7 days, indicating a narrow size distribution (Table S1, Supporting Information). SEM micrographs showed that the Hb@HP-UiO-66-PEG NPs retained their spherical morphology and size in PBS after 2 days, with no visible structural damage (Figure 6c). Similar morphological stability was observed in DMEM, although the images were less distinct due to interference from DMEM components (Figure **S31**, Supporting Information).

Compared to their non-PEGylated counterparts (Hb@HP-UiO-66-NH_2 NPs), Hb@HP-UiO-66-PEG NPs exhibited significantly enhanced stability across all tested solutions. Such an improvement is attributed to the chemical robustness and shielding effect provided by the surface-conjugated PEG layer.[54,55] While approaches to enhance the colloidal stability of MOF-based NPs have been described,[56–59] to the best of our knowledge, this study presents the first successful application of SPAAC-based surface modification to achieve long-term colloidal stability in hierarchically porous MOFs.

3.6. Biocompatibility Assessment of Hb@HP-UiO-66-PEG NPs

Demonstrating biocompatibility is a key factor in HBOCs development for biomedical applications. To assess the biocompatibility of Hb@HP-UiO-66-PEG NPs, we conducted both cytotoxicity and hemocompatibility evaluations. Since macrophages play a crucial role as the body's first line of defense against foreign substances, the RAW 264.7 macrophage cell line was chosen as a model to examine potential cytotoxic effects. These cells were exposed to increasing Hb@HP-UiO-66-PEG NPs concentrations for 24 h at 37 °C, and the nCV was measured in relation to a control group treated with PBS. As illustrated in **Figure 7a**, no significant decrease in nCV was observed at concentrations up to 0.1 mg mL^{-1}. A gradual, concentration-dependent decline became evident as the concentration increased from 0.1 to 1 mg mL^{-1}. Notably, nCV remained above 70% at concentrations up to 0.5 mg mL^{-1}, a threshold commonly regarded as indicative of cytocompatibility according to ISO Standard 10993-5.[60]

Similar concentration-dependent reductions in cell viability have been reported for other MOFs-based HBOCs. For instance, Pan at el., demonstrated that treatment with Hb-loaded ZIF-90-based NPs led to a gradual decline in the viability of human umbilical vein endothelial cells (HUVECs) and b.End3 cells, reaching a nCV of approximately 70% at concentrations of 3 and 0.064 mg mL^{-1}, respectively.[61] These findings highlight the importance of cell line selection in cytotoxicity assessments, as reflected by a more than 40-fold difference in sensitivity. Similarly, Gu at el. reported that Hb-loaded ZIF-8-based NPs decreased HUVECs viability to only ~40% with a concentration of just 0.2 mg mL^{-1} and caused near-complete cell death at 0.5 mg mL^{-1}.[62] In contrast, our previous work showed that Hb-loaded ZIF-8 NPs were non-cytotoxic to RAW 264.7 macrophages at concentrations as high as 2 mg mL^{-1}.[63] This enhanced cytocompatibility is likely due to the negative surface charge of the ZIF-8 NPs, which may reduce interactions with cell membranes. Given the simplicity and versatility of the surface covalent PEGylation strategy used in this study, future work could focus on optimizing the PEG architecture and tuning surface charge to further improve cytocompatibility. Nevertheless, Hb@HP-UiO-66-PEG NPs already demonstrate superior performance compared to PCN-333(Al) NPs the only other reported MOF-based NPs where Hb is entrapped by a similar post-encapsulation approach. Hb-loaded PCN-333(Al) NPs—the only other reported MOF-based system using a similar post-encapsulation method for Hb loading. Specifically, Hb-loaded PCN-333(Al) NPs exhibited a maximum non-toxic concentration of just 0.125 mg mL^{-1} in RAW 264.7 cells,[43] which is significantly lower than the 0.5 mg mL^{-1} achieved with of Hb@HP-UiO-66-PEG NPs (0.5 mg mL^{-1}).

To assess hemocompatibility—an essential criterion for intravenously administered materials—the interaction of Hb@HP-UiO-66-PEG NPs with human RBCs was examined, alongside their effects on plasma coagulation and complement activation. Hemolysis, quantified by measuring the release of Hb from potentially lysed RBCs after 3 h incubation

with varying Hb@HP-UiO-66-PEG NPs concentrations at 37 °C, remained below 2% for all tested concentrations (up to 1 mg mL^{-1}) (Figure 7b). This is also a critical finding as biomaterials are classified as hemolytic if their hemolysis rate exceeds 5%.[64,65] This result was corroborated by visual inspection of the supernatants, which showed no color change indicative of Hb release except in the positive control (Figure 7c). Bright field microscopy further supported hemocompatibility, as RBC morphology remained intact following incubation with NPs, consistent with the negative control (Figure **S32**, Supporting Information). Next, the impact of Hb@HP-UiO-66-PEG NPs on blood coagulation was evaluated using PT and aPTT assays. An increase in PT could indicate interference with clotting factors involved in the extrinsic and common pathways, potentially heightening bleeding risk, whereas a PT reduction might suggest prothrombotic tendencies. As depicted in Figure 7d, NP exposure induced a slight PT prolongation at all tested concentrations compared to the negative control. However, the changes remained within the acceptable reference range (STA®-NeoPTimal, 12.3–15.1 s), except for a minor increase observed at the highest concentration of 1 mg mL^{-1} (15.4 ± 0.7 s). Similarly, aPTT values remained within the normal range (STA®-PPT Automate 5, 29.1–41.9 s) at all concentrations, except at the highest concentration, where a slight elevation was observed (Figure 7e). Despite these modest shifts, Hb@HP-UiO-66-PEG NPs did not significantly disrupt coagulation at the tested concentrations. We attribute this favorable profile to the PEGylated surface of the NPs, which likely forms a hydrophilic barrier that minimizes interactions with blood components involved in initiating coagulation cascades.[66] Supporting this hypothesis, our previous work showed that PEG-coated Hb-loaded ZIF-8 NPs maintained PT and aPTT values within physiological ranges at concentrations up to 2 mg mL^{-1}, whereas their non-PEGylated counterparts caused significant aPTT prolongation even at just 0.2 mg mL^{-1}.[37] Building on these findings, we conclude that Hb@HP-UiO-66-PEG NPs display a favorable hemocompatibility profile,

causing minimal with plasma clotting mechanisms due to their stable, covalently shell formed via SPAAC chemistry.

Approximately 7% of individuals are susceptible to complement-mediated reactions to nanomedicines, with an estimated 0.3% risk of fatality.[38] Thus, due to its potential to trigger immune responses, assessing undesired complement activation is a key consideration for intravenously administered nanomaterials. Complement activation occurs via three primary pathways: the classical (antigen-antibody complex-mediated), alternative (pathogen-mediated), and mannose-binding lectin pathways, all of which produce C5a—key mediator of complement-induced immune responses.[38] For that, we examined whether Hb@HP-UiO-66-PEG NPs at a concentration of 1 mg mL^{-1} stimulated protein C5a expression in human plasma.[67,68] Plasma treated with zymosan (0.2 mg mL^{-1}), a known complement activator, served as a positive control, while PBS-treated plasma functioned as a negative control. As illustrated in Figure 7f, C5a expression showed a slight but statistically insignificant increase following NP exposure, in stark contrast to the pronounced activation seen with zymosan. This suggests that Hb@HP-UiO-66-PEG NPs do not substantially trigger complement activation or provoke immune responses. These findings are consistent with the favorable hemolysis and coagulation profiles observed earlier, as both parameters are closely linked to complement activation.[69,70] Moreover, the minimal immune activation aligns with the known ability of PEGylated NPs to suppress inflammatory responses commonly associated with the injection of foreign materials,[71] further supporting the rational design of Hb@HP-UiO-66-PEG NPs for intravenous applications.

In summary, these results demonstrate that Hb@HP-UiO-66-PEG NPs exhibit strong biocompatibility, reinforcing their potential for further in vivo studies.

3.7. Pharmacokinetics and Biodistribution Studies

Understanding the PK and biodistribution of Hb-loaded NPs after i.v. administration is critical for evaluating their therapeutic potential and efficacy as HBOCs. Free Hb exhibits significant limitations as an HBOC due to its rapid clearance from the bloodstream, where it binds haptoglobin to form a complex that is quickly recognized and cleared by Kupffer cells in the liver via the CD163 scavenger receptor.[72] Additionally, tetrameric Hb dissociates into smaller dimers and monomers, which are readily filtered by renal glomeruli and excreted in the urine.[2] These challenges limit the efficacy of free Hb in therapeutic applications.

In contrast, nanoparticulated HBOCs offer several advantages, including enhanced circulation times. Encapsulation of Hb within NPs prevents its dissociation into smaller subunits, thereby reducing renal clearance and prolonging its presence in the bloodstream.[72] This encapsulation also enhances therapeutic efficacy by ensuring sustained Hb availability in circulation.

Thus, we next evaluated the in vivo performance of Hb@HP-UiO-66-PEG NPs and their potential as HBOCs by investigating their PK profile and organ distribution. To this end, fluorescently labeled Hb^{Cy7} was encapsulated into HP-UiO-66-N_3 NPs to form Hb^{Cy7}@HP-UiO-66-N_3 NPs (Figure **S33**, Supporting Information), followed by surface PEGylation to yield Hb^{Cy7}@HP-UiO-66-PEG NPs. These NPs were administered intravenously to healthy CD-1 mice at a dose of 10 mg/kg (based on total NP weight). Plasma FI was measured at various time points and correlated with a standard curve to determine plasma concentrations of Hb^{Cy7}@HP-UiO-66-PEG NPs (Figure **S34**, Supporting Information). The resulting plasma concentration–time profile, including blood circulation half-life and overall drug exposure, is shown in **Figure 8**. Pharmacokinetic parameters were determined using noncompartmental analysis and are summarized in **Table S2** (Supporting Information). As illustrated in Figure 8a, the PK profile of Hb^{Cy7}@HP-UiO-66-PEG NPs exhibited a biphasic clearance pattern, characterized by an initial rapid elimination phase within the first 6 h, followed by a slower,

sustained clearance phase. The calculated elimination half-life ($t_{1/2\beta}$) was 9.22 ± 1.92 h. This is comparable to previously reported data for free Hb^{Cy7} in the same mouse model, which also followed a biphasic clearance pattern but with a shorter $t_{1/2\beta}$ of 7.65 ± 0.97 h.[37]

These results are in line with other studies on MOF-based HBOCs. For instance, Peng et al., reported that free Hb exhibited a $t_{1/2\beta}$ of only 5.1 h, whereas encapsulation within ZIF-8 NPs extended the circulation half-life to 13.9 h.[19] This is foundational study demonstrated for the first time that MOFs can effectively improve the blood retention of Hb. More recently, our group showed that PEGylation further enhances circulation time: PEG-coated Hb-loaded ZIF-8 NPs achieved a prolonged $t_{1/2\beta}$ of 14.8 h, nearly doubling that of free Hb.[37] The critical role of PEG density in determining circulation time has also been highlighted by Xu et al., who reported a strong positive correlation between PEG content and half-life for Hb-loaded poly(lactic acid) NPs.[73] Specifically, increasing PEG content from 5 to 20 wt% extended the half-life from 0.32 to 34.3 h. Taken together, these findings suggest that both Hb encapsulation within nanoscale UiO-66 and subsequent PEGylation act synergistically to enhance blood retention.

To investigate the organ clearance of produced NPs, we assessed the biodistribution of fluorescently labeled Hb^{Cy7}@HP-UiO-66-PEG NPs following i.v. administration in healthy CD-1 mice at a dose of 10 mg kg^{-1}. As shown in Figure 8b and 8c, the fluorescence signals (e-/s/sr) revealed the accumulation of NPs in key organs, including the liver, kidneys, brain, heart, lungs, spleen, and intestines, at various time points (0.5, 1, 4, 8, and 24 h). Upon injection, the NPs predominantly accumulated in the liver and, to a lesser extent, in the kidneys, suggesting that hepatic routes and renal filtration are the primary pathways for their clearance. These results were in line that observed for free Hb^{Cy7}. It is also well-established that NPs, following i.v. administration, are often sequestered by organs of the mononuclear phagocyte system, such as the liver and spleen, due to interactions with opsonins, which promote subsequent

endocytosis by phagocytic cells.[72] Notably, our results also showed an increase in renal sequestration of Hb^{Cy7}@HP-UiO-66-PEG NPs at later time points. This is likely due to the degradation of NPs into smaller fragments, which are then cleared *via* urinary excretion during prolonged circulation, consistent with findings reported for other NP systems.[73]

These findings highlight the potential advantages of nanoparticulated HBOCs, particularly in overcoming the rapid clearance and renal filtration limitations associated with free Hb. The prolonged blood retention of Hb@HP-UiO-66-PEG NPs suggests enhanced therapeutic potential, as it may improve circulation time and increase efficacy in O_2 delivery. Overall, these results underscore the importance of continued research into the safety and functional performance of Hb@HP-UiO-66-PEG NPs *in vivo*, which could significantly advance the development of these Hb-NPs as effective HBOCs.

4. CONCLUSIONS

In this work, we successfully engineered a physiologically stable, biocompatible, and functionally efficient HBOC using hierarchically porous UiO-66 NPs. The incorporation of mesopores was achieved through a controlled self-assembly process involving Zr^{4+}, a limited supply of BDC ligand and a sacrificial alkyl monocarboxylic acid. This hierarchical porosity facilitated efficient Hb encapsulation while preserving its O_2-carrying capacity. To further enhance physiological stability and biocompatibility, we employed a catalyst-free click-chemistry surface modification approach for PEGylation. This strategy significantly improved colloidal stability in physiological media, reduced immune recognition—as indicated by the absence of complement activation—and ensured excellent hemocompatibility and cell viability. *In vivo* pharmacokinetic and biodistribution analyses demonstrated extended blood retention and favorable organ accumulation patterns for Hb@HP-UiO-66-PEG NPs compared to free Hb. These findings mark a significant step toward overcoming the limitations of existing HBOCs and highlight the potential of HP-UiO-66 NPs as synthetic RBC substitutes for

therapeutic O_2 delivery. Future research will focus on optimizing these nanocarriers for clinical applications, ensuring their safety and efficacy in transfusion medicine and critical care.

AUTHOR INFORMATION

Corresponding Author

* E-mail: leri@dtu.dk

Declaration of generative AI and AI-assisted technologies in the writing process

During the preparation of this work the authors used Chat GPT in order to improve the readability of the manuscript. After using this tool/service, the authors reviewed and edited the content as needed and take full responsibility for the content of the publication.

ACKNOWLEDGMENT

This research was funded by the European Research Council under the European Union's Horizon 2020 Research and Innovation Program (Grant No. 101002060). The authors gratefully thank Bodil Fliis Holten (Department of Chemistry, Technical University of Denmark) for assistance in preliminary N_2 measurement. The authors also appreciate Marlene Danner Dalgaard and Lotte Nielsen (Department of Health Technology, Technical University of Denmark) for their help with human blood withdrawal and instrument training, respectively. The authors thank Clara Coll-Satue, Despoina Douka and Mohammadsadegh Nadimifar (Department of Health Technology, Technical University of Denmark) for introducing Weiguang to the hemolysis assay, hemoglobin extraction, and O_2 meter, respectively.

REFERENCES

[1] J.S. Jahr, N.R. Guinn, D.R. Lowery, L. Shore-Lesserson, A. Shander, Blood Substitutes and Oxygen Therapeutics: A Review, Anesth. Analg. 132 (2021) 119–129. https://doi.org/10.1213/ANE.0000000000003957.

[2] M.M.T. Jansman, L. Hosta-Rigau, Recent and prominent examples of nano- and microarchitectures as hemoglobin-based oxygen carriers, Adv. Colloid Interface Sci. 260 (2018) 65–84. https://doi.org/10.1016/j.cis.2018.08.006.

[3] C. Gao, Z. Lin, D. Wang, Z. Wu, H. Xie, Q. He, Red Blood Cell-Mimicking Micromotor for Active Photodynamic Cancer Therapy, ACS Appl. Mater. Interfaces 11 (2019) 23392–23400. https://doi.org/10.1021/acsami.9b07979.

[4] J. Chen, X. Liu, M.M.T. Jansman, P.W. Thulstrup, L. Hosta-Rigau, Metal-Phenolic Networks as Broad-Spectrum Antioxidant Coatings for Hemoglobin Nanoparticles Working as Oxygen Carriers, Chem. Mater. 34 (2022) 9200–9211. https://doi.org/10.1021/acs.chemmater.2c02190.

[5] C. Coll-Satue, S. Bishnoi, J. Chen, L. Hosta-Rigau, Stepping stones to the future of haemoglobin-based blood products: clinical, preclinical and innovative examples, Biomater. Sci. 9 (2021) 1135–1152. https://doi.org/10.1039/D0BM01767A.

[6] K. Taguchi, T. Maruyama, M. Otagiri, Pharmacokinetic properties of hemoglobin vesicles as a substitute for red blood cells, Drug Metab. Rev. 43 (2011) 362–373. https://doi.org/10.3109/03602532.2011.558094.

[7] S. Rameez, H. Alosta, A.F. Palmer, Biocompatible and Biodegradable Polymersome Encapsulated Hemoglobin: A Potential Oxygen Carrier, Bioconjugate Chem. 19 (2008) 1025–1032. https://doi.org/10.1021/bc700465v.

[8] M. O. Pacheco, H. M. Lutz, J. Armada, N. Davies, I. K. Gerzenshtein, A. S. Cakley, B. D. Spiess, W. L. Stoppel, Silk Fibroin Particles as Carriers in the Development of Hemoglobin-Based Oxygen Carriers, Adv. Nanobiomed Res. 3 (2023) 2300019. https://doi.org/org/10.1002/anbr.202300019.

[9] Y. Taguchi, Y. Cu, J. Fei, L. Dai, J. Li, Yang, Construction and Evaluation of Hemoglobin-BasedCapsules as Blood Substitutes, Adv. Funct. Mater. 22 (2012) 1446–1453. https://doi.org/10.1002/adfm.201102737.

[10] C. Coll-Satue, M.M.T. Jansman, P.W. Thulstrup, L. Hosta-Rigau, Optimization of Hemoglobin Encapsulation within PLGA Nanoparticles and Their Investigation as Potential Oxygen Carriers, Pharmaceutics 13 (2021) 1958. https://doi.org/10.3390/pharmaceutics13111958.

[11] M.M.T. Jansman, C. Coll-Satue, X. Liu, P.J. Kempen, T.L. Andresen, P.W. Thulstrup, L. Hosta-Rigau, Hemoglobin-based oxygen carriers camouflaged with membranes extracted from red blood cells: Optimization and assessment of functionality, Biomater. Adv. 134 (2022) 112691. https://doi.org/10.1016/j.msec.2022.112691.

[12] X. Liu, M.M.T. Jansman, L. Hosta-Rigau, Haemoglobin-loaded metal organic framework-based nanoparticles camouflaged with a red blood cell membrane as potential oxygen delivery systems, Biomater. Sci. 8 (2020) 5859–5873. https://doi.org/10.1039/D0BM01118e.

[13] Z. Wang, J. Chen, R. Gao, L. Jiang, G. Zhang, Y. Zhao, Y.-B. Miao, Y. Shi, Spatiotemporal manipulation metal–organic frameworks as oral drug delivery systems for precision medicine, Coord. Chem. Rev. 502 (2024) 215615. https://doi.org/10.1016/j.ccr.2023.215615.

[14] H.D. Lawson, S.P. Walton, C. Chan, Metal–Organic Frameworks for Drug Delivery: A Design Perspective, ACS Appl. Mater. Interfaces 13 (2021) 7004–7020. https://doi.org/10.1021/acsami.1c01089.

[15] X. Lian, Y.-P. Chen, T.-F. Liu, H.-C. Zhou, Coupling two enzymes into a tandem nanoreactor utilizing a hierarchically structured MOF, Chem. Sci. 7 (2016) 6969–6973. https://doi.org/10.1039/C6SC01438K.

[16] M.B. Majewski, A.J. Howarth, P. Li, M.R. Wasielewski, J.T. Hupp, O.K. Farha, Enzyme encapsulation in metal–organic frameworks for applications in catalysis, CrystEngComm 19 (2017) 4082–4091. https://doi.org/10.1039/C7CE00022G.

[17] W. Jin, X. Li, S.M. Argandona, R.M. Ray, M.K.T.H. Lin, F. Melle, G. Clergeaud, T. Lars Andresen, M. Nielsen, D. Fairen-Jimenez, K. Astakhova, K. Qvortrup, Surface engineering of metal-organic framework nanoparticles-based miRNA carrier: Boosting RNA stability, intracellular delivery and synergistic therapy, J. Colloid Interface Sci. 677 (2025) 429–440. https://doi.org/10.1016/j.jcis.2024.08.074.

[18] S. Peng, B. Bie, Y. Sun, M. Liu, H. Cong, W. Zhou, Y. Xia, H. Tang, H. Deng, X. Zhou, Metal-organic frameworks for precise inclusion of single-stranded DNA and transfection in immune cells, Nat. Commun. 9 (2018) 1293. https://doi.org/10.1038/s41467-018-03650-w.

[19] S. Peng, J. Liu, Y. Qin, H. Wang, B. Cao, L. Lu, X. Yu, Metal–Organic Framework Encapsulating Hemoglobin as a High-Stable and Long-Circulating Oxygen Carriers to Treat Hemorrhagic Shock, ACS Appl. Mater. Interfaces 11 (2019) 35604–35612. https://doi.org/10.1021/acsami.9b15037.

[20] Q. Wang, J. Gong, Q. Bai, Y. Qin, X. Zhou, M. Wu, H. Ji, L. Wu, Hemoglobin coated oxygen storage metal–organic framework as a promising artificial oxygen carrier, J. Mater. Chem. B 9 (2021) 4002–4005. https://doi.org/10.1039/D1TB00328C.

[21] K. Li, J. Yang, J. Gu, Hierarchically Porous MOFs Synthesized by Soft-Template Strategies, Acc. Chem. Res. 55 (2022) 2235–2247. https://doi.org/10.1021/acs.accounts.2c00262.

[22] K. Liang, R. Ricco, C.M. Doherty, M.J. Styles, S. Bell, N. Kirby, S. Mudie, D. Haylock, A.J. Hill, C.J. Doonan, P. Falcaro, Biomimetic mineralization of metal-organic frameworks as protective coatings for biomacromolecules, Nat. Commun. 6 (2015) 7240. https://doi.org/10.1038/ncomms8240.

[23] G. Cheng, W. Li, L. Ha, X. Han, S. Hao, Y. Wan, Z. Wang, F. Dong, X. Zou, Y. Mao, S.-Y. Zheng, Self-Assembly of Extracellular Vesicle-like Metal–Organic Framework Nanoparticles for Protection and Intracellular Delivery of Biofunctional Proteins, J. Am. Chem. Soc. 140 (2018) 7282–7291. https://doi.org/10.1021/jacs.8b03584.

[24] M.D.J. Velásquez-Hernández, E. Astria, S. Winkler, W. Liang, H. Wiltsche, A. Poddar, R. Shukla, G. Prestwich, J. Paderi, P. Salcedo-Abraira, H. Amenitsch, P. Horcajada, C.J. Doonan, P. Falcaro, Modulation of metal-azolate frameworks for the tunable release of encapsulated glycosaminoglycans, Chem. Sci. 11 (2020) 10835–10843. https://doi.org/10.1039/D0SC01204A.

[25] F.-K. Shieh, S.-C. Wang, C.-I. Yen, C.-C. Wu, S. Dutta, L.-Y. Chou, J.V. Morabito, P. Hu, M.-H. Hsu, K.C.-W. Wu, C.-K. Tsung, Imparting Functionality to Biocatalysts via Embedding Enzymes into Nanoporous Materials by a *de Novo* Approach: Size-Selective Sheltering of Catalase in Metal–Organic Framework Microcrystals, J. Am. Chem. Soc. 137 (2015) 4276–4279. https://doi.org/10.1021/ja513058h.

[26] S.K. Alsaiari, S. Patil, M. Alyami, K.O. Alamoudi, F.A. Aleisa, J.S. Merzaban, M. Li, N.M. Khashab, Endosomal Escape and Delivery of CRISPR/Cas9 Genome Editing Machinery Enabled by Nanoscale Zeolitic Imidazolate Framework, J. Am. Chem. Soc. 140 (2018) 143–146. https://doi.org/10.1021/jacs.7b11754.

[27] H. Feng, Z. Li, W. Xie, Q. Wan, Y. Guo, J. Chen, J. Wang, X. Pei, Delivery of therapeutic miRNAs using nanoscale zeolitic imidazolate framework for accelerating vascularized bone regeneration, Chem. Eng. J. 430 (2022) 132867. https://doi.org/10.1016/j.cej.2021.132867.

[28] C. Coll-Satue, M. Rubio-Huertas, A. Ducrot, E. Norkute, X. Liu, F.M. Ebrahim, B. Smit, P.W. Thulstrup, L. Hosta-Rigau, A novel PEG-mediated approach to entrap hemoglobin (Hb) within ZIF-8 nanoparticles: Balancing crystalline structure, Hb content and functionality, Biomater. Adv. 163 (2024) 213953. https://doi.org/10.1016/j.bioadv.2024.213953.

[29] D. Douka, W. Jin, C. Cantallops-Iglesias, A. Dieste-Izquierdo, P.W. Thulstrup, L. Hosta-Rigau, Optimization and Investigation of Hemoglobin-Loaded ZIF-90 Metal–Organic Framework Nanoparticles as Artificial Oxygen Carriers, Part. Part. Syst. Charact. 42 (2025). https://doi.org/10.1002/ppsc.202400189.

[30] G. Cai, H.-L. Jiang, A Modulator-Induced Defect-Formation Strategy to Hierarchically Porous Metal–Organic Frameworks with High Stability, Angew. Chem. Int. Ed. 56 (2017) 563–567. https://doi.org/10.1002/anie.201610914.

[31] S. Wen, Q. Fu, L. Yan, X. Zhao, Hierarchically porous three-dimensional-ordered macro-microporous metal-organic frameworks: Design, precise synthesis, and applications, Coordination Chemistry Reviews 517 (2024) 215996. https://doi.org/10.1016/j.ccr.2024.215996.

[32] N. Siegel, H. Hasebe, G. Chiarelli, D. Garoli, H. Sugimoto, M. Fujii, G.P. Acuna, K. Kołątaj, Universal Click-Chemistry Approach for the DNA Functionalization of Nanoparticles, J. Am. Chem. Soc. 146 (2024) 17250–17260. https://doi.org/10.1021/jacs.4c03833.

[33] Z. Wang, S. Hu, J. Yang, A. Liang, Y. Li, Q. Zhuang, J. Gu, Nanoscale Zr-Based MOFs with Tailorable Size and Introduced Mesopore for Protein Delivery, Adv. Funct. Mater. 28 (2018) 1707356. https://doi.org/10.1002/adfm.201707356.

[34] C. Coll-Satue, M.M.T. Jansman, L. Hosta-Rigau, Comparative Evaluation of UV-Vis Spectroscopy-Based Approaches for Hemoglobin Quantification: Method Selection and Practical Insights, Biomolecules 14 (2024) 1046. https://doi.org/10.3390/biom14091046.

[35] S. Øien, D. Wragg, H. Reinsch, S. Svelle, S. Bordiga, C. Lamberti, K.P. Lillerud, Detailed Structure Analysis of Atomic Positions and Defects in Zirconium Metal–Organic Frameworks, Cryst.Growth Des. 14 (2014) 5370–5372. https://doi.org/10.1021/cg501386j.

[36] J.W.M. Osterrieth, J. Rampersad, D. Madden, N. Rampal, L. Skoric, B. Connolly, M.D. Allendorf, V. Stavila, J.L. Snider, R. Ameloot, J. Marreiros, C. Ania, D. Azevedo, E. Vilarrasa-Garcia, B.F. Santos, X. Bu, Z. Chang, H. Bunzen, N.R. Champness, S.L. Griffin, B. Chen, R. Lin, B. Coasne, S. Cohen, J.C. Moreton, Y.J. Colón, L. Chen, R. Clowes, F. Coudert, Y. Cui, B. Hou, D.M. D'Alessandro, P.W. Doheny, M. Dincă, C. Sun, C. Doonan, M.T. Huxley, J.D. Evans, P. Falcaro, R. Ricco, O. Farha, K.B. Idrees, T. Islamoglu, P. Feng, H. Yang, R.S. Forgan, D. Bara, S. Furukawa, E. Sanchez, J. Gascon, S. Telalović, S.K. Ghosh, S. Mukherjee, M.R. Hill, M.M. Sadiq, P. Horcajada, P. Salcedo-Abraira, K. Kaneko, R. Kukobat, J. Kenvin, S. Keskin, S. Kitagawa, K. Otake, R.P.

Lively, S.J.A. DeWitt, P. Llewellyn, B.V. Lotsch, S.T. Emmerling, A.M. Pütz, C. Martí-Gastaldo, N.M. Padial, J. García-Martínez, N. Linares, D. Maspoch, J.A. Suárez Del Pino, P. Moghadam, R. Oktavian, R.E. Morris, P.S. Wheatley, J. Navarro, C. Petit, D. Danaci, M.J. Rosseinsky, A.P. Katsoulidis, M. Schröder, X. Han, S. Yang, C. Serre, G. Mouchaham, D.S. Sholl, R. Thyagarajan, D. Siderius, R.Q. Snurr, R.B. Goncalves, S. Telfer, S.J. Lee, V.P. Ting, J.L. Rowlandson, T. Uemura, T. Iiyuka, M.A. Van Der Veen, D. Rega, V. Van Speybroeck, S.M.J. Rogge, A. Lamaire, K.S. Walton, L.W. Bingel, S. Wuttke, J. Andreo, O. Yaghi, B. Zhang, C.T. Yavuz, T.S. Nguyen, F. Zamora, C. Montoro, H. Zhou, A. Kirchon, D. Fairen-Jimenez, How Reproducible are Surface Areas Calculated from the BET Equation?, Adv.Mater. 34 (2022) 2201502. https://doi.org/10.1002/adma.202201502.

[37] G. Bor, W. Jin, D. Douka, N.J. Borthwick, X. Liu, M.M.T. Jansman, L. Hosta-Rigau, In vitro and in vivo investigations of hemoglobin-loaded PEGylated ZIF-8 nanoparticles as oxygen carriers for emergency transfusion, Biomater. Adv. 168 (2025) 214118. https://doi.org/10.1016/j.bioadv.2024.214118.

[38] N. Maisha, M. Rubenstein, C.J. Bieberich, E. Lavik, Getting to the Core of It All: Nanocapsules to Mitigate Infusion Reactions Can Promote Hemostasis and Be a Platform for Intravenous Therapies, Nano Lett. 21 (2021) 9069–9076. https://doi.org/10.1021/acs.nanolett.1c02746.

[39] J. Liu, T.-Y. Bao, X.-Y. Yang, P.-P. Zhu, L.-H. Wu, J.-Q. Sha, L. Zhang, L.-Z. Dong, X.-L. Cao, Y.-Q. Lan, Controllable porosity conversion of metal-organic frameworks composed of natural ingredients for drug delivery, Chem. Commun. 53 (2017) 7804–7807. https://doi.org/10.1039/C7CC03673F.

[40] P. Horcajada, T. Chalati, C. Serre, B. Gillet, C. Sebrie, T. Baati, J.F. Eubank, D. Heurtaux, P. Clayette, C. Kreuz, J.-S. Chang, Y.K. Hwang, V. Marsaud, P.-N. Bories, L. Cynober, S. Gil, G. Férey, P. Couvreur, R. Gref, Porous metal–organic-framework nanoscale carriers as a potential platform for drug delivery and imaging, Nat. Mater. 9 (2010) 172–178. https://doi.org/10.1038/nmat2608.

[41] L. Liu, K. Hou, S. Lin, Y. Di, Z. Zhuang, Z. Zeng, Y. Sun, C. Ji, C. Huang, R. Xiong, Hemoglobin based oxygen carrier and its application in biomedicine, Coord. Chem. Rev. 532 (2025) 216508. https://doi.org/10.1016/j.ccr.2025.216508.

[42] X. Liu, M.M.T. Jansman, W. Li, P. Kempen, P.W. Thulstrup, L. Hosta-Rigau, Metal–organic framework-based oxygen carriers with antioxidant protection as a result of a

polydopamine coating, Biomater. Sci. 9 (2021) 7257–7274. https://doi.org/10.1039/D1BM01005K.

[43] X. Liu, N.P. Domingues, E. Oveisi, C. Coll-Satue, M.M.T. Jansman, B. Smit, L. Hosta-Rigau, Metal–organic framework-based oxygen carriers with antioxidant activity resulting from the incorporation of gold nanozymes, Biomater. Sci. 11 (2023) 2551–2565. https://doi.org/10.1039/D2BM01405J.

[44] P. Wiśniewska, J. Haponiuk, M.R. Saeb, N. Rabiee, S.A. Bencherif, Mitigating metal-organic framework (MOF) toxicity for biomedical applications, Chem. Eng. J. 471 (2023) 144400. https://doi.org/10.1016/j.cej.2023.144400.

[45] X. Liu, A. Ortega-Guerrero, N. P. Domingues, M.J. Pougin, B. Smit, L. Hosta-Rigau, C. Oostenbrink, Stability Assessment in Aqueous and Organic Solvents of Metal–Organic Framework PCN 333 Nanoparticles through a Combination of Physicochemical Characterization and Computational Simulations, Langmuir 40 (2024) 21976–21984. https://doi.org/10.1021/acs.langmuir.4c01684.

[46] A. Kamanzi, Y. Gu, R. Tahvildari, Z. Friedenberger, X. Zhu, R. Berti, M. Kurylowicz, D. Witzigmann, J.A. Kulkarni, J. Leung, J. Andersson, A. Dahlin, F. Höök, M. Sutton, P.R. Cullis, S. Leslie, Simultaneous, Single-Particle Measurements of Size and Loading Give Insights into the Structure of Drug-Delivery Nanoparticles, ACS Nano 15 (2021) 19244–19255. https://doi.org/10.1021/acsnano.1c04862.

[47] W. Jia, Y. Wang, R. Liu, X. Yu, H. Gao, Shape Transformable Strategies for Drug Delivery, Adv Funct Materials 31 (2021) 2009765. https://doi.org/10.1002/adfm.202009765.

[48] W. Jin, X. Li, G. Clergeaud, R.M. Ray, M.K.T. Hong Lin, T.L. Andresen, C.H. Gotfredsen, M. Nielsen, K. Astakhova, K. Qvortrup, Small RNA stabilization via non-covalent binding with a metalloporphyrin nanocage to accomplish synergistic gene and photodynamic therapy, Cell Rep. Phys. Sci. 3 (2022) 101187. https://doi.org/10.1016/j.xcrp.2022.101187.

[49] H. Bunzen, Chemical Stability of Metal-Organic Frameworks for Applications in Drug Delivery, ChemNanoMat 7 (2021) 998–1007. https://doi.org/10.1002/cnma.202100226.

[50] D. Bůžek, S. Adamec, K. Lang, J. Demel, Metal–organic frameworks *vs.* buffers: case study of UiO-66 stability, Inorg. Chem. Front. 8 (2021) 720–734. https://doi.org/10.1039/D0QI00973C.

[51] W. Jin, W. Chen, P. Xu, X. Lin, X. Huang, G. Chen, F. Lu, X. Chen, An Exceptionally Water Stable Metal–Organic Framework withAmide-Functionalized Cages: Selective

CO2/CH4 Uptake andRemoval of Antibiotics and Dyes from Water, Chem.Eur.J 23 (2017) 13058–13066. https://doi.org/10.1002/chem.201701884.

[52] J.S. Suk, Q. Xu, N. Kim, J. Hanes, L.M. Ensign, PEGylation as a strategy for improving nanoparticle-based drug and gene delivery, Adv. Drug Deliv. Rev. 99 (2016) 28–51. https://doi.org/10.1016/j.addr.2015.09.012.

[53] P. Andreozzi, C. Simó, P. Moretti, J. Martinez Porcel, T. Ursula Lüdtke, M. de los Angeles Ramirez, L. Tamber, M. Marradi, H. Amenitsch, J. Llop, M. Grazia Ortore, S. Enrique Moya, Novel Core–Shell Polyamine Phosphate Nanoparticles Self-Assembled from PEGylated Poly(allylamine hydrochloride)with Low Toxicity and Increased In Vivo Circulation Time, Small 17 (2021) 2102211. https://doi.org/10.1002/smll.202102211.

[54] X. Chen, S.M. Argandona, F. Melle, N. Rampal, D. Fairen-Jimenez, Advances in surface functionalization of next-generation metal-organic frameworks for biomedical applications: Design, strategies, and prospects, Chem 10 (2024) 504–543. https://doi.org/10.1016/j.chempr.2023.09.016.

[55] M. Giménez-Marqués, E. Bellido, T. Berthelot, T. Simón-Yarza, T. Hidalgo, R. Simón-Vázquez, Á. González-Fernández, J. Avila, M. Carmen Asensio, R. Gref, P. Couvreur, C. Serre, P. Horcajada, GraftFast Surface Engineering to Improve MOF Nanoparticles Furtiveness, Small 14 (2018) 1801900. https://doi.org/10.1002/smll.201801900.

[56] I. Abánades Lázaro, S. Haddad, S. Sacca, C. Orellana-Tavra, D. Fairen-Jimenez, R.S. Forgan, Selective Surface PEGylation of UiO-66 Nanoparticles for Enhanced Stability, Cell Uptake, and pH-Responsive Drug Delivery, Chem 2 (2017) 561–578. https://doi.org/10.1016/j.chempr.2017.02.005.

[57] X. Chen, Y. Zhuang, N. Rampal, R. Hewitt, G. Divitini, C.A. O'Keefe, X. Liu, D.J. Whitaker, J.W. Wills, R. Jugdaohsingh, J.J. Powell, H. Yu, C.P. Grey, O.A. Scherman, D. Fairen-Jimenez, Formulation of Metal–Organic Framework-Based Drug Carriers by Controlled Coordination of Methoxy PEG Phosphate: Boosting Colloidal Stability and Redispersibility, J. Am. Chem. Soc. 143 (2021) 13557–13572. https://doi.org/10.1021/jacs.1c03943.

[58] C. Carrillo-Carrión, V. Comaills, A.M. Visiga, B.R. Gauthier, N. Khiar, Enzyme-Responsive Zr-Based Metal–Organic Frameworks for Controlled Drug Delivery: Taking Advantage of Clickable PEG-Phosphate Ligands, ACS Appl. Mater. Interfaces 15 (2023) 27600–27611. https://doi.org/10.1021/acsami.3c03230.

[59] Y. Zeng, J. Xiao, Y. Cong, J. Liu, Y. He, B.D. Ross, H. Xu, Y. Yin, H. Hong, W. Xu, PEGylated Nanoscale Metal–Organic Frameworks for Targeted Cancer Imaging and

Drug Delivery, Bioconjugate Chem. 32 (2021) 2195–2204. https://doi.org/10.1021/acs.bioconjchem.1c00368.

[60] International Organization for Standardization. ISO 10993: Parts 1–12; ISO: Geneva, Switzerland., (n.d.).

[61] Z.-Q. Pan, S.-L. Yu, Z.-Q. Wu, K. Wang, Construction and Evaluation of Zeolitic Imidazolate Framework-Encapsulated Hemoglobin Microparticles as Oxygen Carriers, ACS Appl. Bio Mater. 6 (2023) 1471–1478. https://doi.org/10.1021/acsabm.2c01013.

[62] X. Gu, M. Allyn, K. Swindle-Reilly, A.F. Palmer, ZIF-8 metal organic framework nanoparticle loaded with tense quaternary state polymerized bovine hemoglobin: potential red blood cell substitute with antioxidant properties, Nanoscale 15 (2023) 8832–8844. https://doi.org/10.1039/D2NR06812e.

[63] C. Coll-Satue, E. Cabrera-San Millan, M.M.T. Jansman, L. Arnholdt, L. Hosta-Rigau, Hemoglobin-loaded ZIF-8 nanoparticles equipped with PEGylated metal-phenolic network coatings: an oxygen carrier with antioxidant and stealth properties, J. Mater. Chem. B 13 (2025) 3374–3389. https://doi.org/10.1039/D4TB01771D.

[64] M. Weber, H. Steinle, S. Golombek, L. Hann, C. Schlensak, H.P. Wendel, M. Avci-Adali, Blood-Contacting Biomaterials: In Vitro Evaluation of the Hemocompatibility, Front. Bioeng. Biotechnol. 6 (2018) 99. https://doi.org/10.3389/fbioe.2018.00099.

[65] ISO/DIS 10993-4(en), Biological evaluation of medical devices — Part 4: Selection of tests for interactions with blood. https://www.iso.org/obp/ui/#iso:std:iso:10993:-4:dis:ed-3:v1:en (accessed 2024-07-01)., (n.d.).

[66] Y. Tian, Z. Gao, N. Wang, M. Hu, Y. Ju, Q. Li, F. Caruso, J. Hao, J. Cui, Engineering Poly(ethylene glycol) Nanoparticles for Accelerated Blood Clearance Inhibition and Targeted Drug Delivery, J. Am. Chem. Soc. 144 (2022) 18419–18428. https://doi.org/10.1021/jacs.2c06877.

[67] N.S. Merle, R. Noe, L. Halbwachs-Mecarelli, V. Fremeaux-Bacchi, L.T. Roumenina, Complement System Part II: Role in Immunity, Front. Immunol. 6 (2015). https://doi.org/10.3389/fimmu.2015.00257.

[68] A. Klos, A.J. Tenner, K.-O. Johswich, R.R. Ager, E.S. Reis, J. Köhl, The role of the anaphylatoxins in health and disease, Mol. Immunol. 46 (2009) 2753–2766. https://doi.org/10.1016/j.molimm.2009.04.027.

[69] O. May, N.S. Merle, A. Grunenwald, V. Gnemmi, J. Leon, C. Payet, T. Robe-Rybkine, R. Paule, F. Delguste, S.C. Satchell, P.W. Mathieson, M. Hazzan, E. Boulanger, J.D. Dimitrov, V. Fremeaux-Bacchi, M. Frimat, L.T. Roumenina, Heme Drives Susceptibility

of Glomerular Endothelium to Complement Overactivation Due to Inefficient Upregulation of Heme Oxygenase-1, Front. Immunol. 9 (2018) 3008. https://doi.org/10.3389/fimmu.2018.03008.

[70] J. Wang, L. Liu, C. Liu, N. Cheng, Q. Mao, C. Chen, J. Hu, H. He, X. Hui, P. Qu, W. Lian, L. Duan, Y. Dong, Y. Liu, J. Li, Identification and analysis of differential miRNA–mRNA interactions in coronary heart disease: an experimental screening approach, Front. Cardiovasc. Med. 10 (2023) 1186297. https://doi.org/10.3389/fcvm.2023.1186297.

[71] K.L. Lee, S. Shukla, M. Wu, N.R. Ayat, C.E. El Sanadi, A.M. Wen, J.F. Edelbrock, J.K. Pokorski, U. Commandeur, G.R. Dubyak, N.F. Steinmetz, Stealth filaments: Polymer chain length and conformation affect the in vivo fate of PEGylated potato virus X, Acta Biomater. 19 (2015) 166–179. https://doi.org/10.1016/j.actbio.2015.03.001.

[72] K. Taguchi, K. Yamasaki, T. Maruyama, M. Otagiri, Comparison of the Pharmacokinetic Properties of Hemoglobin-Based Oxygen Carriers, J. Funct. Biomater. 8 (2017) 11. https://doi.org/10.3390/jfb8010011.

[73] Y. Sheng, Y. Yuan, C. Liu, X. Tao, X. Shan, F. Xu, In vitro macrophage uptake and in vivo biodistribution of PLA–PEG nanoparticles loaded with hemoglobin as blood substitutes: effect of PEG content, J. Mater. Sci. Mater. Med. 20 (2009) 1881–1891. https://doi.org/10.1007/s10856-009-3746-9.

FIGURES

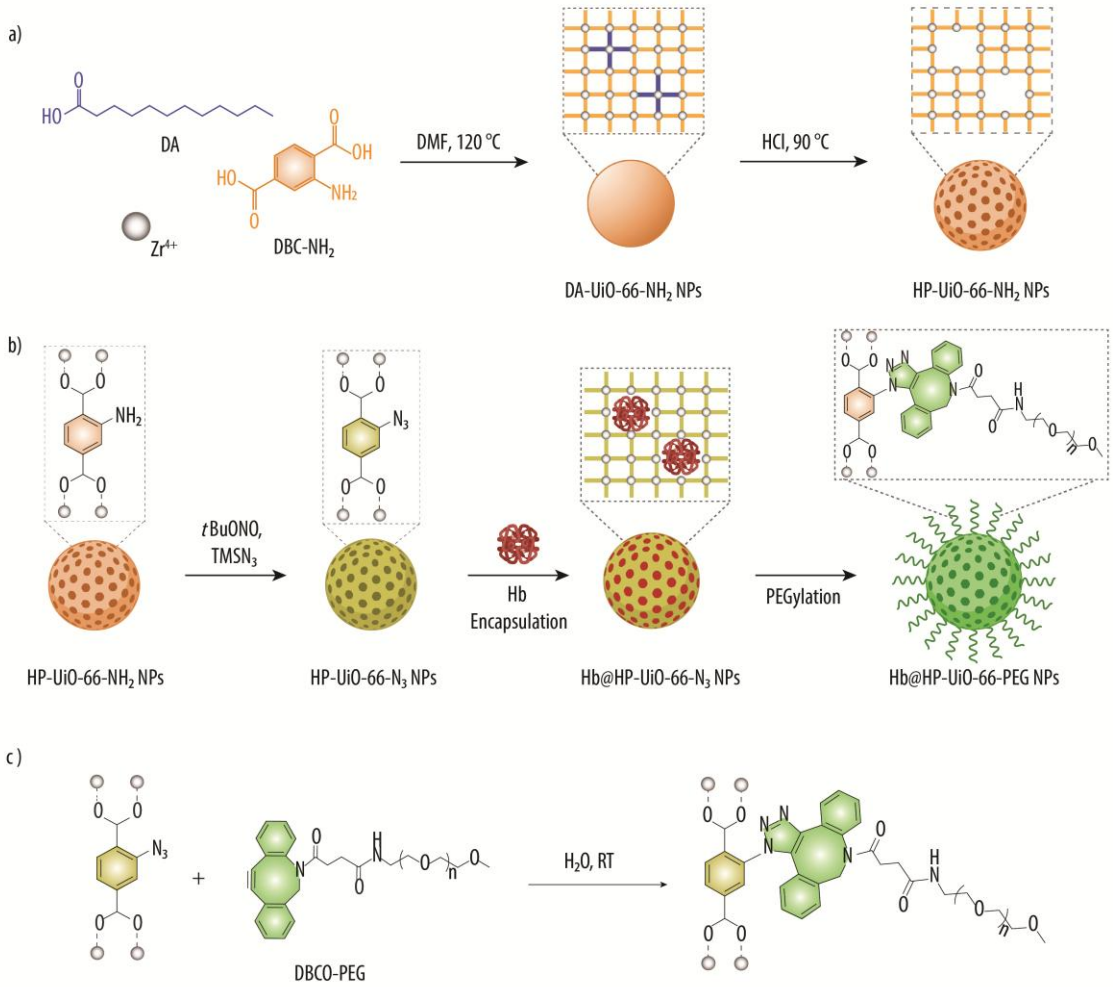

Schematic 1. a) DA-UiO-66-NH_2 NPs are fabricated by the solvothermal reaction of DBC-NH_2, DA and Zr^{4+} in DMF at 120 °C. HP-UiO-66-NH_2 NPs are obtained after DA removal by acidic treatment. **b)** HP-UiO-66-NH_2 NPs are reacted with *t*BuONO and $TMSN_3$ rendering azide-modified HP-UiO-66-N_3 NPs. After Hb encapsulation, the resulting Hb@HP-UiO-66-N_3 NPs are surface PEGylated. **c)** PEGylated Hb@HP-UiO-66-PEG NPs is achieved by SPAAC, which can be conducted with PEG-modified DBCO-PEG under ambient conditions.

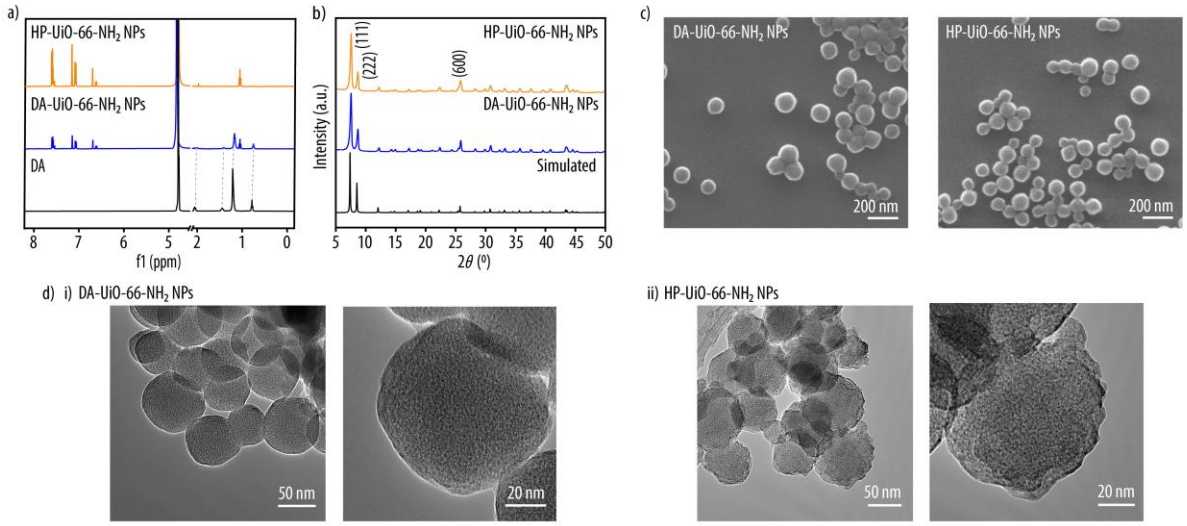

Figure 1. a) ^{1}H NMR spectra of DA, DA-UiO-66-NH_2 and HP-UiO-66-NH_2 NPs. **b)** Simulated diffractogram of UiO-66 and PXRD patterns of DA-UiO-66-NH_2 and HP-UiO-66-NH_2 NPs. **c)** SEM images of DA-UiO-66-NH_2 and HP-UiO-66-NH_2 NPs. **d)** TEM images of **i)** DA-UiO-66-NH_2 and **ii)** HP-UiO-66-NH_2 NPs.

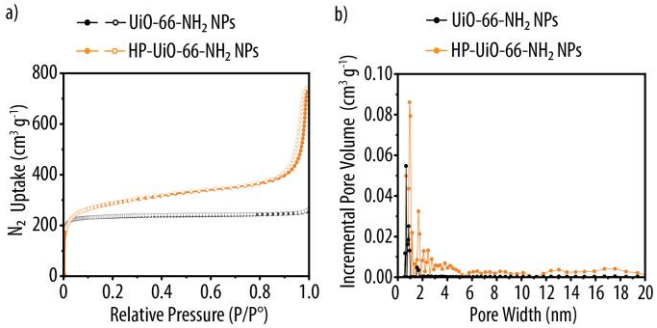

Figure 2. a) N_2 adsorption-desorption isotherms and **b**) the corresponding pore size distributions of UiO-66-NH_2 and HP-UiO-66-NH_2 NPs.

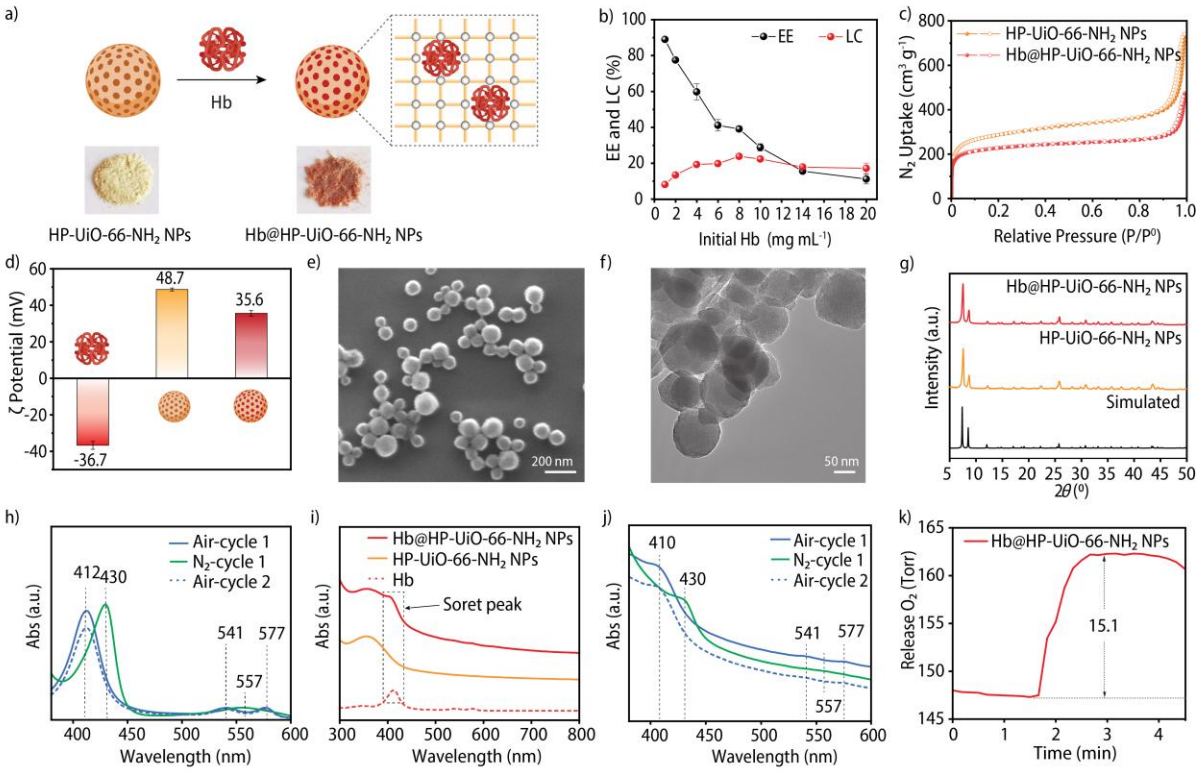

Figure 3. a) Schematic illustration of Hb encapsulation into HP-UiO-66-NH_2 NPs to render Hb@HP-UiO-66-NH_2 NPs including photographs of the NPs powder before and after encapsulation; **b**) EE and LC of Hb encapsulation to render Hb@HP-UiO-66-NH_2 NPs; **c**) N_2 adsorption-desorption isotherms of HP-UiO-66-NH_2 and Hb@HP-UiO-66-NH_2 NPs; **d**) ζ-potential of free Hb, HP-UiO-66-NH_2 and Hb@HP-UiO-66-NH_2 NPs; **e**) SEM and **f**) TEM of Hb@HP-UiO-66-NH_2 NPs; **g**) PXRD of simulated UiO-66, HP-UiO-66-NH_2 and Hb@HP-UiO-66-NH_2 NPs; **h**) UV-vis spectra of free Hb following purging with N_2 and compressed for several cycles; **i**) UV-vis spectra of free Hb, HP-UiO-66-NH_2 and Hb@HP-UiO-66-NH_2 NPs; **j**) UV-vis spectra of Hb@HP-UiO-66-NH_2 NPs following purging with N_2 and compressed air for several cycles; **k**) O_2 released from Hb@HP-UiO-66-NH_2 NPs.

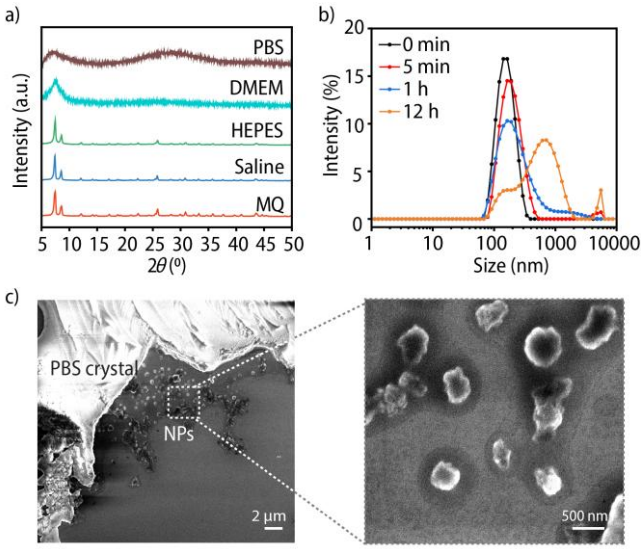

Figure 4. **a**) PXRD of Hb@HP-UiO-66-NH_2 NPs after incubation in various physiologically relevant solvents for 24 h at 37 °C; **b**) Time-solved DLS of Hb@HP-UiO-66-NH_2 NPs in PBS; **c**) SEM images of Hb@HP-UiO-66-NH_2 NPs after 2 h exposure PBS incubation.

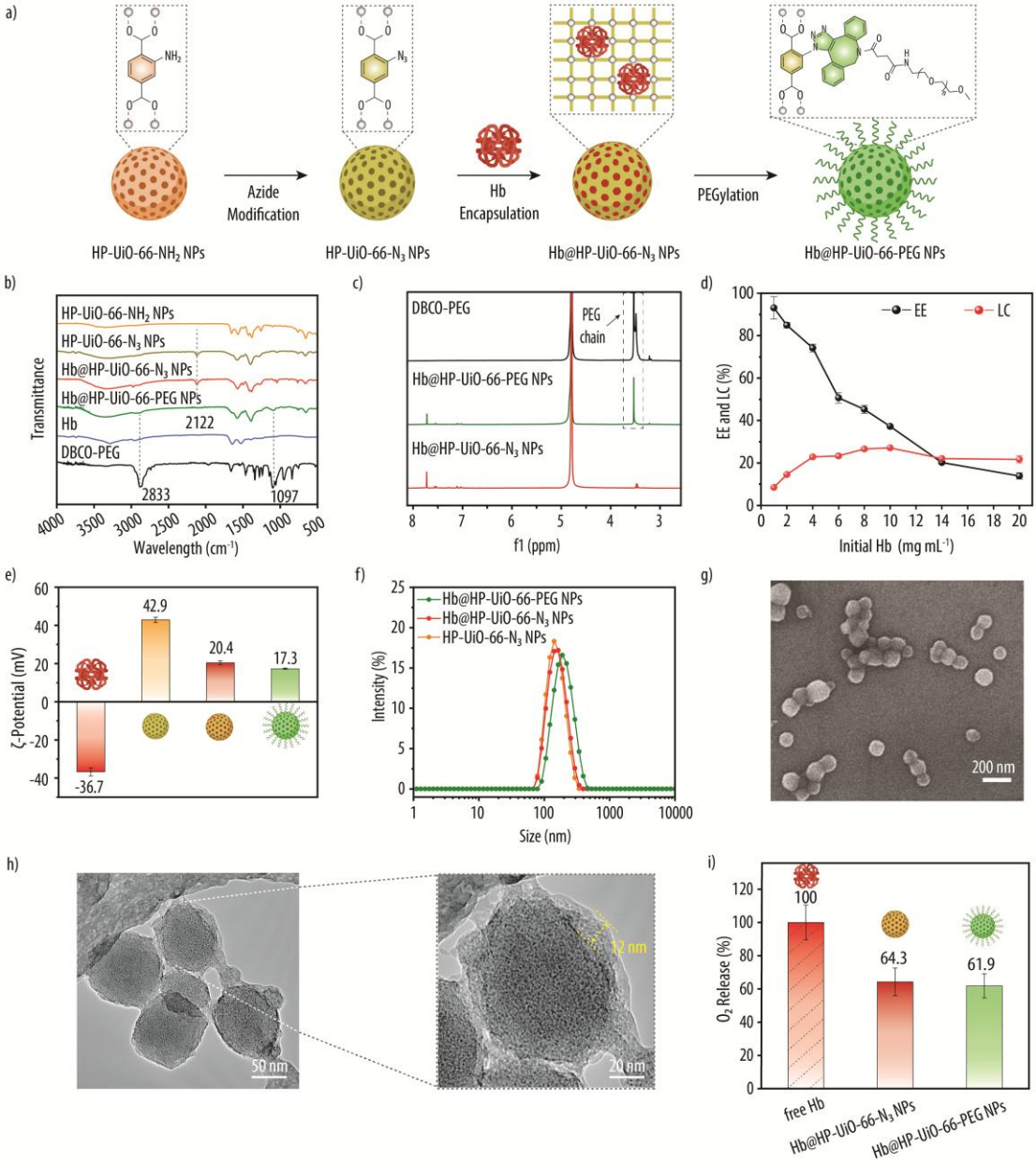

Figure 5. a) Schematic illustration of the fabrication of Hb@HP-UiO-66-PEG NPs, including azide modification, Hb encapsulation and PEGylation; **b**) FTIR of NPs at each synthesis step, free Hb and DBCO-PEG reagent; **c**) ^{1}H NMR spectra of DBCO-PEG, Hb@HP-UiO-66-N_3 and Hb@HP-UiO-66-PEG NPs; **d**) EE and LC of Hb encapsulation for Hb@HP-UiO-66-N_3 NPs; **e**) ζ-potential and **f**) DLS of HP-UiO-66-N_3, Hb@HP-UiO-66-N_3 and Hb@HP-UiO-66-PEG NPs; **g**) SEM and **h**) TEM images of Hb@HP-UiO-66-PEG NPs (yellow arow indicating

the PEG layer surrounding the NPs); **i**) O_2 released by Hb@HP-UiO-66-N_3 and Hb@HP-UiO-66-PEG NPs relative to free Hb.

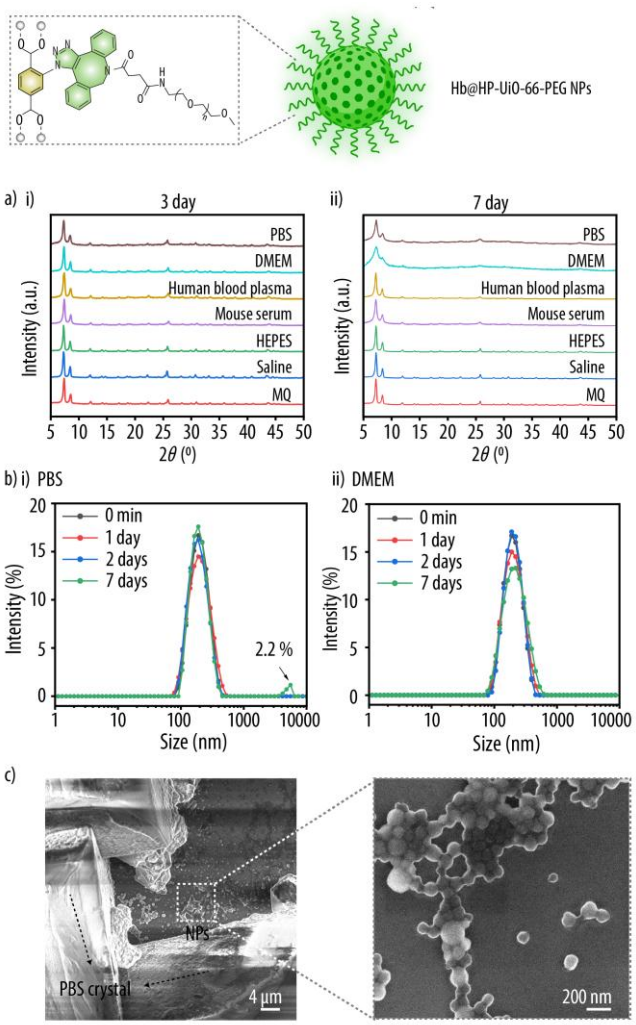

Figure 6. a) PXRD of Hb@HP-UiO-66-PEG NPs after incubation in various physiologically relevant solvents at 37 °C for **i**) 3 and **ii**) 7 days; **b**) DLS of Hb@HP-UiO-66-PEG NPs after incubation in **i**) PBS and **ii**) DMEM for up to 7 days; **c**) SEM image of Hb@HP-UiO-66-PEG NPs after 48 h PBS incubation at 37 °C.

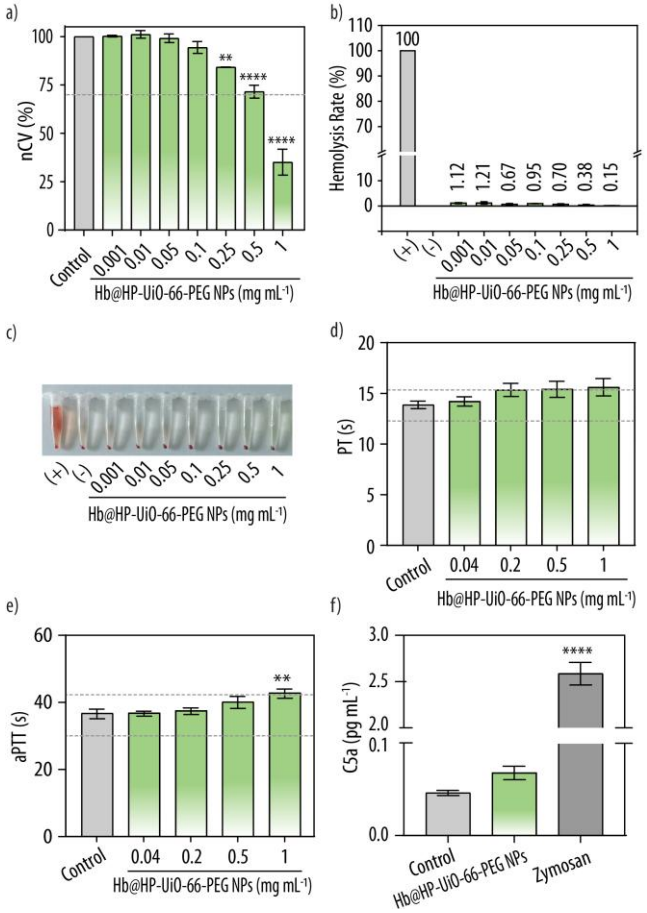

Figure 7. a) nCV of RAW 264.7 cells after 24 h incubation with increasing concentrations of Hb@HP-UiO-66-PEG NPs. The grey dashed line indicates 70% nCV. **b**) Hemolysis rate of RBC after being incubated for 3 h with increasing concentrations of Hb@HP-UiO-66-PEG NPs and **c**) the corresponding photographic images. RBCs incubated with MQ and PBS only were used as positive (+) and negative (−) controls, respectively. Effect Hb@HP-UiO-66-PEG NPs on **d)** PT and **e)** aPTT. Plasma incubated with PBS serves as a control. The grey dashed lines represent the corresponding STA ® -NeoPTimal reference intervals: 12.3 – 15.1 s for PT and 29.1 – 41.9 s for aPTT. **f**) Effect of Hb@HP-UiO-66-PEG NPs at a concentration of 1 mg mL^{-1} on the soluble complement marker C5a compared to control (PBS). Zymosan at a concentration of 0.2 mg mL^{-1} was used as positive control. Statistical significance was determined by one-way ANOVA using GraphPad Prism 10 followed by the Kruskal-Wallis multiple comparison tests test (*p<0.05, **p<0.005, ***p<0.001, ****p<0.0001).

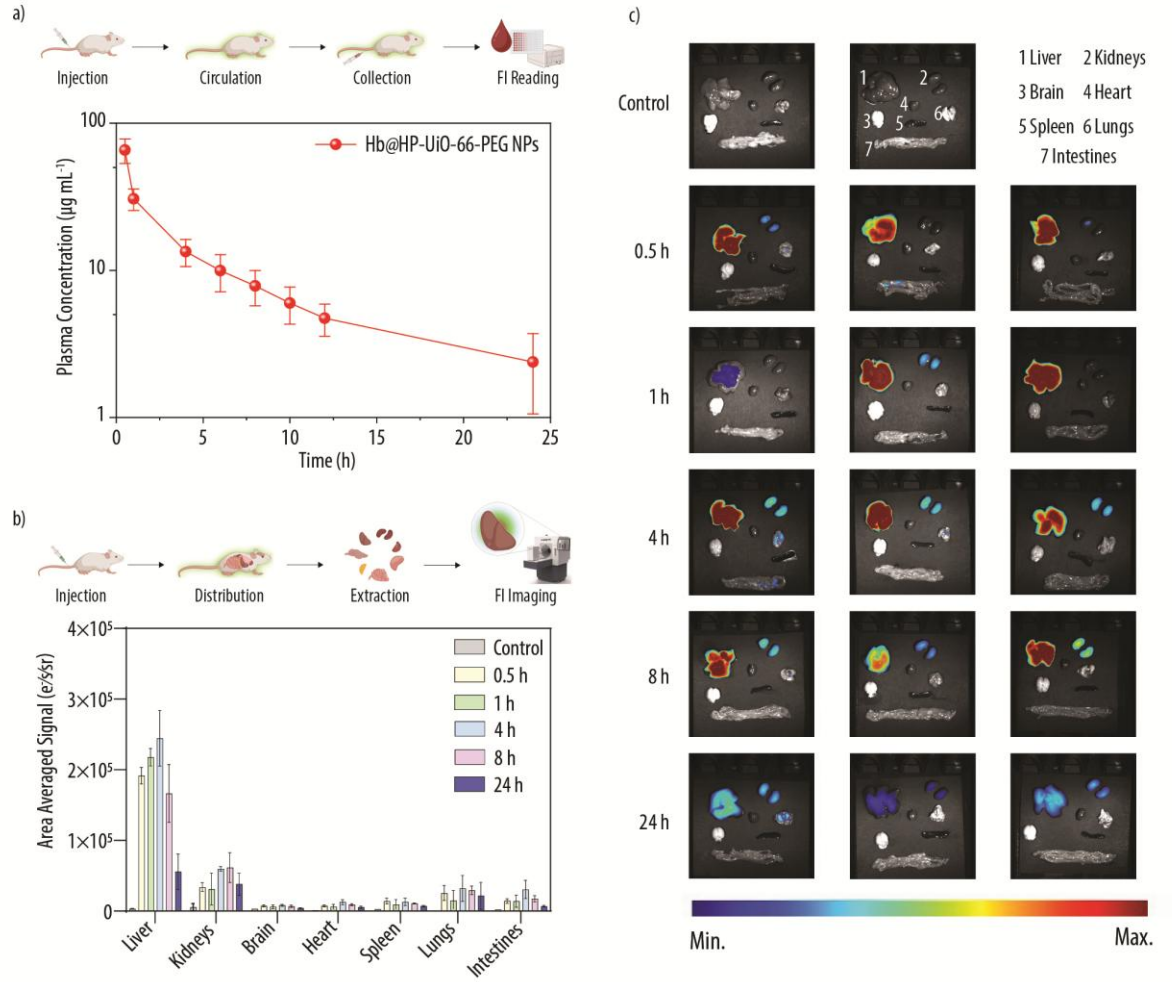

Figure 8. a) Blood circulation profiles of free Hb and PEGylated NPs Hb@HP-UiO-66-PEG NPs after intravenous administration at dose of 10 mg kg^{-1} to healthy CD-1 mice (n = 3 per group); **b**) biodistribution of intravenously injected of Hb@HP-UiO-66-PEG NPs in healthy CD-1 mice determined by ex vivo imaging using a fluorescence molecular tomography device. The accumulation of NPs was determined by the fluorescent quantification in organs (liver, kidneys, brain, heart, lungs, spleen, and intestines) at different post-injection times (n = 3 per group and per time point). Data expressed as of averaged signals (e-/s/sr) and presented as mean ± SD; **c**) the corresponding images of organs with fluorescent intensity to show the *ex vivo* distribution of the Hb@HP-UiO-66-PEG NPs.

Graphic abstract

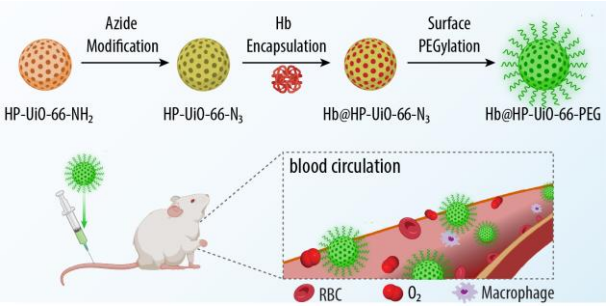

Timely blood transfusion is critical for preventing hypoxia, yet it faces limitations in availability, storage, and compatibility. Herein hierarchically porous metal-organic framework nanoparticles with surface covalent PEGylation were developed for carrying hemoglobin, offering promising red blood cell substitutes with enhanced stability, biocompatibility, and prolonged circulation for oxygen delivery.